2017-10-01

Semiconductor Terahertz Electronics and Novel High-Speed Single-Shot Measurements

Parker Dean Salmans
Brigham Young University

Semiconductor Terahertz Electronics and Novel

High-Speed Single-Shot Measurements

Parker Dean Salmans

A thesis submitted to the faculty of
Brigham Young University
in partial fulfillment of the requirements for the degree of

Master of Science

Jeremy A. Johnson, Chair
James E. Patterson
Karl Warnick

Department of Chemistry and Biochemistry

Brigham Young University

ABSTRACT

Semiconductor Terahertz Electronics and Novel
High-Speed Single-Shot Measurements

Parker Dean Salmans
Department of Chemistry and Biochemistry, BYU
Master of Science

Ultrafast spectroscopy is used to study essential characteristics of solid-state materials. We use ultrafast techniques to study semiconductors at THz frequencies, as well as demonstrate new single-shot measurement techniques. The future of electronics is in the THz regime. We study a crucial characteristic of semiconductors used in devices: the critical field at which the material becomes conductive. GaAs is a promising semiconductor for high-speed devices, and we use enhanced THz electric fields to measure the critical fields at 0.7, 0.9, 1.1, and 1.5 THz frequencies. Single-shot spectroscopy is a technique used to measure ultrafast time scale laser pulses. We show that a new, optical-fiber-based single-shot technique can map out the electric field of THz pulses. Also, we show two variants on this single-shot theme that can be used to measure ultrafast signals. We compare a classic pump-probe measurement to two types of single-shot measurements that use either a spectrometer or a 3 km fiber optic cable and oscilloscope, and we discuss important considerations to recovering the sample response.

Keywords: THz, Critical Field, Single-shot Probing

Acknowledgments

Many people deserve acknowledgement for the publication of this thesis. I hope I can do justice to how grateful I am to all the people that influenced me and assisted me in my graduate student experience.

I would first like to say thank you to my professor, Jeremy Johnson. Dr. Johnson deserves all the praise in the world, not only is he a great scientist, a genius, and great at his job, he is also one of the most kind and charitable men I know. He has guided me through difficulties and problems both in the lab and in my life. I can't say thank you enough for his kindness and ability to inspire. Many times I would be on the verge of walking out of the lab and leaving for good, only for Dr. Johnson to come in and, with a few words, inspire me to double down and try even harder. Dr. Johnson has provided so many opportunities for growth and learning. Truly, all I can say is thank you for it all, sincerely. I would also like to thank the fabulous members of the Johnson Spectroscopy Lab. By name, I would like to thank Nick Ellsworth for being my brother and partner on both of my research projects. I would also like to thank Larry Heki for his tireless efforts in helping me learn matlab and for being someone I could always turn to for help. Next, I would like to thank all of the professors here at BYU who gave me encouragement and help in my research and classes.

My family has been a big support and help in completing this master's degree and I would like to say thank you and I love you. My parents have always been anchors to which I can use to steady my life during difficult days. A big thank you to my mom and dad for their love and support always. I knew I always had someone to talk to and work through difficult problems during my time here.

Lastly, but not least, I would like to acknowledge the moral support and endless

encouragement, love, and inspiration my dear wife, Sydney, has given me. She has always been a pillar in my life, especially in the hectic and stressful time as a graduate student. I always knew that at the end of the day there would be a smiling face to lift me up and inspire me to keep going. To my dear wife, I love you and cannot say thank you enough. I would also like to say thank you to my wonderful children. They are my inspiration and motivation for working hard and continuing forward.

Table of Contents

List of Figures

Chapter 1

Introduction to Ultrafast Spectroscopy

A simple definition of spectroscopy is how light interacts with the physical world. Some of the earliest scientific developments involved light-based observations. As spectroscopic techniques have advanced from their early beginnings, time-resolved measurements have become a pillar of scientific discovery – using light to watch how processes evolve in time. The history of using light to measure physical phenomena is rich with interesting and relevant developments that continue to shape our world. The first measurement of its kind, to observe motion faster than a human eye can track, is now known as the stroboscopic horse. This measurement was done by a fellow named Eadweard Muybridge, formerly known as Edward Muggeridge. Eadweard was originally from England, and at 20 years of age and hungry for adventure, he traveled to America where he changed his name and began doing work for Leland Stanford, the founder of Stanford University. Leland was an avid horse racer and wished to know if at any point in a horse's stride, all four legs left the ground at the same time. This was unknown because human vision is not fast enough (not enough time-resolution) to capture all the information needed to answer this question. Eadweard took the challenge and devised a clever experiment where he would have a horse race around a track that had trip cords attached to cameras. The triggered cameras recorded a fast exposure, essentially creating freeze-frame

pictures of the horse's motion at that moment, corresponding to various moments in its stride as it galloped around the track [1]. The resulting recorded images are shown in Figure 1.1.
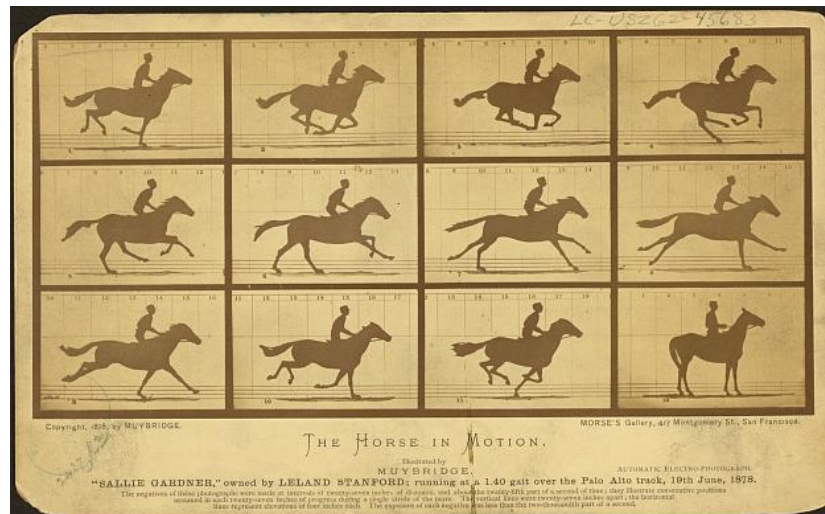

Figure 1.1: The Horse in Motion as first reported by Eadward Muybridge. This innovative stroboscopic technique was able to capture motion faster than our eyes can capture. [1]

We see in the 2nd and 3rd panels of Figure 1.1 that horses do in fact have moments where all four hooves are off the ground. More importantly it introduced the world of science to taking time-resolved measurements faster than the human eye can respond. Stroboscopic probing allows one to observe the evolution of a sample as it changes in time by taking fast snap-shot pictures at delayed times.

With shorter or better time resolution, you can observe faster and faster motion. Many dynamics on the atomic level happen much faster than a horse galloping on the racetrack; therefore, it takes flashes of light at shorter time scales to be able to capture these processes. For the ultimate, fastest observations, the time resolution is related to how short a flash or pulse of light you can create. With the invention of the laser, researchers started to push the pulse duration to shorter and shorter times to investigate phenomenon that happened at shorter and

shorter time scales. From microseconds to nanoseconds to picoseconds, continual instrumental

developments led to laser pulse durations shrinking in time. Thus, ultrafast techniques were born

allowing the study of processes on picosecond or shorter timescales. Examples of processes that

happen on this time scale include electron dynamics or nuclear vibrations. Motions such as these

require time resolution on picosecond (10^{-12} s) to femtosecond (10^{-15} s) time scales.

A variety of lasers have been invented that can generate such short pulses of light: these

include fiber lasers, dye lasers, semiconductor lasers and bulk lasers. The laser pulse duration,

pulse repetition rate and pulse energy can be controlled for each experiment. Each type of laser

has its own mechanism of producing short pulses of light. In our lab, a bulk Ti:Sapphire laser is

used. Bulk lasers usually are made of a solid state material that has electronic transitions

available in the wavelength range of interest, for example, 1050 nm for Nd:YAG lasers and 800

nm for Ti:Sapphire lasers. These lasers utilize unique features known as mode-locking and

dispersion compensation to create the ultrafast lasers we use to investigate interesting

phenomena. Mode-locking is a method of designing the cavity of your laser to match up with

specific modes in the repetition rate of the laser to produce the most gain and most powerful

pulse energy pulse.   Ti:Sapphire lasers implement mode-locking in the length of the cavity. Our

laser locks on the TEM00 mode to optimize the output. As the light makes round trips in the

cavity the other modes are killed off. Short pulses of light necessarily have a broad spectrum,

which can lead to dispersion-induced stretching of the pulses. A dispersion grating is used to

compensate for any amplification stretching that happens in the medium. This allows for

stretched pulses to be recompressed to the femtosecond duration needed for ultrafast

measurements.

In pump-probe measurements, different wavelengths of light can be used as the pump or probe. The pump can be used to excite a transition and the probe can probe that same transition or a different one depending on the wavelength. Using different wavelengths or studying your sample with different energy can reveal new discoveries and new insights. Exciting samples with differing amounts of energy can let us see different things happen within the sample. As an example, light in the visible range is often used to excite electronic transitions [2], light in the IR range to excited vibrations [3], and light in the microwave range can be used to excite rotations of molecular samples [4]. Higher energy light into the UV and X-ray range has also been used in pump-probe measurements to excite high energy transitions and atomic processes [5]. The technique of pump-probe is truly a field that has many avenues and areas of study.

As an example of an ultrafast pump-probe measurement, we will discuss electro-optic sampling [6], which is a THz pump-800 nm probe measurement we use to measure a THz waveform with its associated electric field strength. 800-nm pulses of light generated by our Ti:Sapphire laser are split into pump and probe lines. In THz-pump measurements, the pump portion of the 800-nm light is converted to an IR wavelength light (often 1450 nm) using an optical parametric amplifier, which is then directed into a THz generation crystal, as shown in Figure 1.2. In the THz generation crystal, the IR light generates broadband pulses of THz radiation through the process of optical rectification.

When intense light pulses, like the 1450 nm we use, are incident on a non-centrosymmetric crystal, the electronic response has an asymmetric component. When optical rectification happens and the electrons change direction in the crystal, the moving charge produces a relatively low frequency electric field in the THz frequency range.
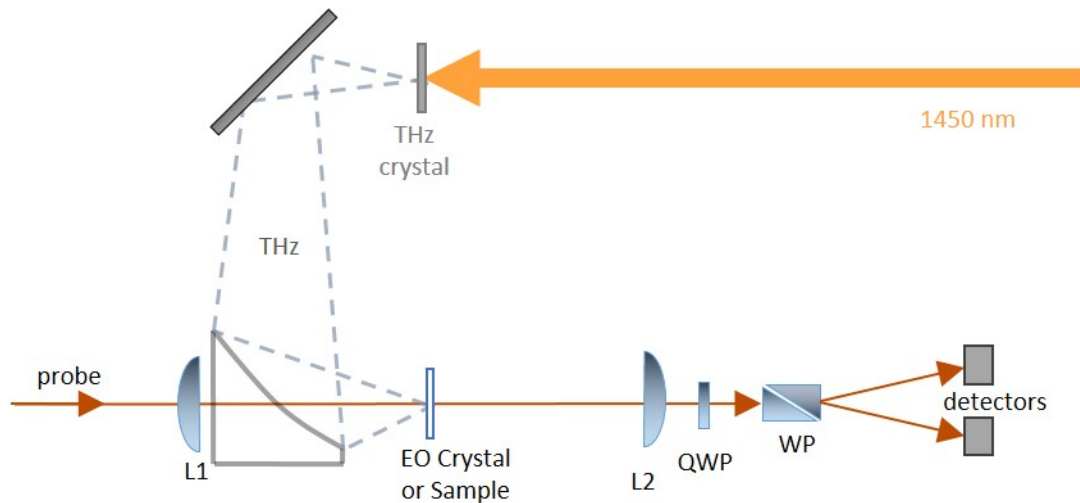
Figure 1.2: Example of a traditional THz pump-optical probe measurement. 1450 nm light is converted to THz radiation in the THz generation crystal. The THz is directed to and focused on the sample. L1 is lens that focusses the probe to the sample position and L2 re-collimates the beam. QWP is a λ/4-waveplate and WP is a Wollaston prism used to convert polarization rotation into intensity changes read out by the balanced detectors.

High intensity, short pulses of light are critical in optical rectification generation of THz radiation and the crystal which is used has the largest (induced) polarization possible. Optical rectification is a non-linear process that is caused by the high intensity of the IR light we pump the crystal with. Having a large nonlinear polarization causes larger electronic motion, leading to high THz electric fields.

The probe line is much simpler. The 800-nm light from the laser is directed to and focused onto the sample. Within that probe line is a mobile stage that can be adjusted to make the optical path length longer or shorter, changing the relative timing between arrival of the probe pulse and the pump pulse at the sample position. Once the pump and probe lines are lined up in both space and time, we vary the probe timing to record the THz electric field as it passes through the crystal. For further explanation, see Figure 3.1B and the associated text in Chapter 3. The probe pulses are short enough duration to map out the THz electric field as it passes through

5

the electro-optic crystal, typically GaP in our lab [6]. Fundamentally, the electro-optic effect is a nonlinear coupling between a low frequency electric field (terahertz pulse) and a laser beam (optical pulse) in the sensor crystal. All of the electric fields and polarizations interact in the EO crystal to produce the signal.

The fact that the electric field induces birefringence is the key to the measurement. With an applied electric field (the THz pulse), the crystal has different refractive indices for different directions in the crystal, and the two different polarization components of our incoming light are relatively delayed in time with respect to each other, making the light elliptically polarized. The amount of ellipticity of the probe pulse can be measured as the light is sent through a $\lambda/4$ waveplate and Wollaston prism, which convert the polarization rotation into changes in amplitude that can be measured on balanced photodiodes. The magnitude of the ellipticity of the is probe pulse is determined by the interaction of the THz pump pulse with the EO crystal, as it will modulate the refractive index in the crystal [6]. Therefore, we can recover absolute electric field strengths and how the THz electric field varies in time.

High-field THz generation is still a fairly new technique in comparison to many of the other wavelength ranges that are used in pump-probe measurements. This is an engaging route of investigation because many of the degrees of freedom that can be excited with THz are still yet to be explored.

My two projects focused on two aspects of these pump-probe measurements. One project focused on using the pump-probe measurements in the form of THz transmission experiments to examine electron behavior in semiconductors at THz frequencies. The other is focused on improving and exploring the pump-probe technique to make single-shot measurements faster, more efficient, and cheaper. We will begin by exploring in Chapter 2 some of the fundamentals

to electron dynamics in semiconductors. In Chapter 3, we will present our research of THz electron behavior in semiconductors and we determine critical field of GaAs at THz frequencies. In Chapter 4, we will review various types of pump-probe measurements and a newer, faster version of single-shot probing. In Chapter 5, we compare two variants of single-shot probing, how we used two detection techniques to improve measurements, and we discuss important considerations to recovering the sample response in such measurements.

Chapter 2

Introduction into Field-Driven Electron Dynamics in Semiconductors

There is a constant push to develop faster electronic devices. For example, current computer processors operate at GHz frequencies, with the fastest Intel processor rated at 3.6 GHz. Current research is aimed at pushing these computation speeds up to even THz frequencies, which would allow computers to run thousands of times faster than the existing state-of-the-art. In order to develop such high-speed technologies, we must understand excited carrier dynamics in semiconductors at THz frequencies. Excited carriers are electrons that have been excited into the conduction band through a variety of ways. We will explore the important carrier dynamics in semiconductors promising for high speed applications using high field THz radiation.

Semiconductors are variable in conductivity because there is a bandgap between the electronic energy bands that arise from the highest occupied molecular orbital (HOMO) and lowest occupied molecular orbital (LOMO) that make up the semiconductor. In a crystalline structure, the atomic energy levels combine to make molecular orbitals. In solids, these molecular orbitals are called electronic bands, and give the allowed energy levels that electrons can occupy. In a conductive metal, the electronic band structure is such that the highest energy valence band overlaps (in energy) with the lowest energy conduction band. In other words, the

conduction band which is unoccupied is not energetically separated from the valence band which is occupied by electrons; therefore, the electrons are free to move into the conduction band of the crystal, and once in the conduction band, can flow freely throughout the material, therefore making the metal conductive to electrical currents. In an insulating material, just the opposite is true. The valence and conduction band are separated in energy and so the valence band electrons are not as easily able to be excited into the conduction band under normal conditions, and therefore can't travel freely across the crystal.

One should be aware that electronic band-structures are complex functions of energy and wavevector. Band gaps are defined in terms of wavevector (and the associated wavelength) according to the Bloch-theorem. This theory describes electrons in crystals as waves and as such, each electron has a specific momentum connected with its de Broglie wavelength. The electronic band structure plotted in Figure 2.1 is a plot of how energy and momentum behave in the GaAs crystal constrained to specific values. The wavevector point labeled Γ is the starting point of the unit cell of the crystal (corresponding to the lowest electron momentum). As we increase the wavevector in the X (100) direction, the allowed energies change dependent on the wavevector. Moving in the L (111) direction of the crystal, the bands change energetically differently than in the X (or any other) direction. The band gap is defined as the energy difference between the lowest energy point of the conduction band in the wavevector space and the highest energy point of the valence band, for any wavevector in the wavevector space. As discussed below, this can be at the same point (as in direct gap semiconductors as in GaAs shown in Figure 2.1) or not at the same wavevector (as in indirect gap semiconductors like silicon).
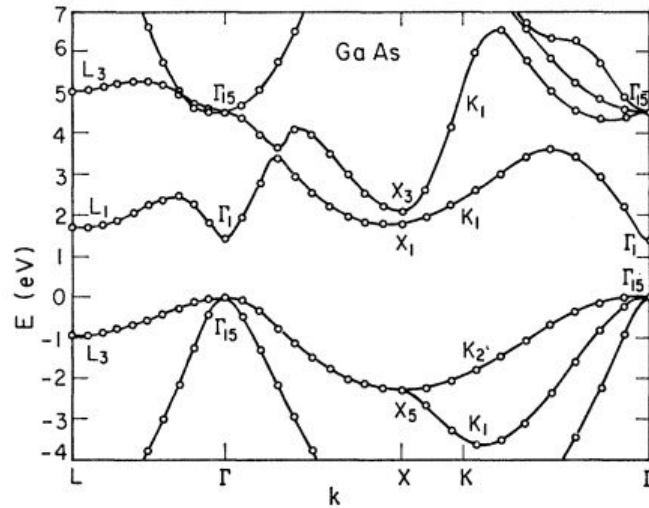
9

Figure 2.1: The full band gap diagram of gallium arsenide (GaAs), with bandgap of 1.42 eV. The valence band is fully populated at low temperatures, and when electrons are excited into the conduction band, electrons can flow freely through the crystal. [7]

Semiconductors are often grouped into different classes based on the shape of their electronic band structure as well as the magnitude of their electronic band gap. One such semiconductor classification is based on the wavevector space at which the bandgap falls. Many times, the lowest point in the conduction band and the highest point in the valence band will be at the same point in the vector space of the crystal. When this happens, as shown in Figure 2.1 for GaAs, the semiconductor is termed a direct bandgap semiconductor. If there is no bandgap, this definition fits for a metal (the metal valence and conduction bands overlap at the Γ point). If the low point and high point of the conduction and valence band respectively do not line up at the same wavevector, it is an indirect bandgap semiconductor. Similarly, if there is no bandgap, but the high valence and low conduction bands don't line up in wavevector space, it is called a semimetal. Figure 2.2 shows simplified depictions of these four types of electronic band structures.
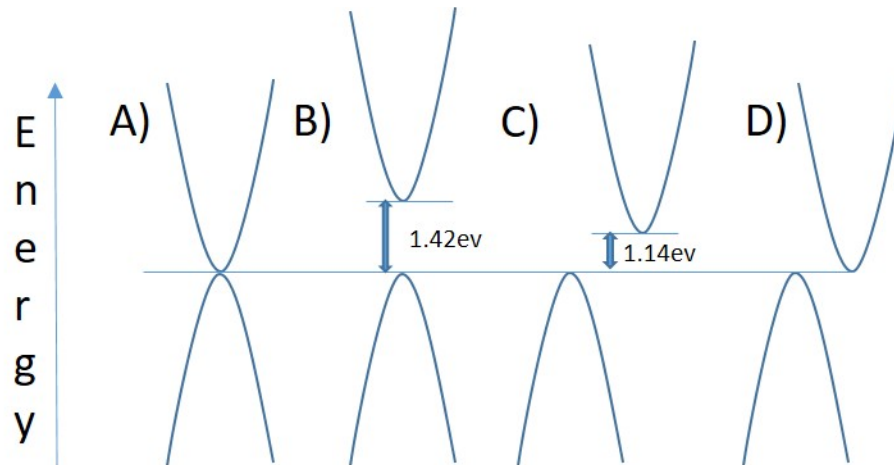
10

Figure 2.2 Above is shown the four standard types of band gaps we can find in solid materials. A) Depicted is a metal where the valence band and conduction band are touching and there is no energy barrier between the two. B) The bandgap of gallium arsenide which is a direct bandgap semiconductor with a bandgap of 1.42 meV. C) Silicon as an indirect semiconductor which has a bandgap of 1.14 eV which takes additional steps to excite electrons into the conduction band compared to a direct band semiconductor. D) An indirect metal or semimetal where there is no energy gap but the bands are indirect in vector space.

Semiconductors with a bandgap below 0-1 eV, which 1 eV is equal to 241 THz in frequency corresponding to 124 μm in wavelength, are known as short or narrow bandgap semiconductors. Narrow bandgap semiconductors are often very easy to excite electrons into the conduction band and become conducting due to the small bandgap. Semiconductors with a bandgap energy between 1-2 eV are normal semiconductors. Semiconductors with a bandgap >2 eV are classified as a wide bandgap semiconductor [8]. Examples of these types of semiconductors for narrow band are lead telluride (0.25 eV) and indium arsenide (0.354 eV), the more common and most used fall in the normal category including silicon (1.14 eV) and gallium arsenide (1.42 eV), finally wide bandgap semiconductors include gallium nitride (3.4 eV) and diamond (5.47 eV).

11

The process of exciting electrons can be accomplished in a variety of ways. When an electron has been excited into the conduction band, a hole is left in the valence band. This hole is the lack of negative charge that was once there, leaving a positive charge in the valence band that behaves like a particle with an effective mass. One straightforward way of exciting electrons to the conduction band is to simply heat up the semiconductor, therefore adding energy to the valence band electrons such that some have enough thermal energy to be excited across the bandgap. This can lead the conductivity of the semiconductor to increase as shown in Figure 2.3 [10]. The green line shows how for silicon, a common semiconductor, the conductivity increases at higher temperature. In a metal like tungsten, however, electronic states in the conduction band will begin to saturate with more thermal energy due to the Pauli exclusion principle. This in turn causes the conductivity of the tungsten to decrease.
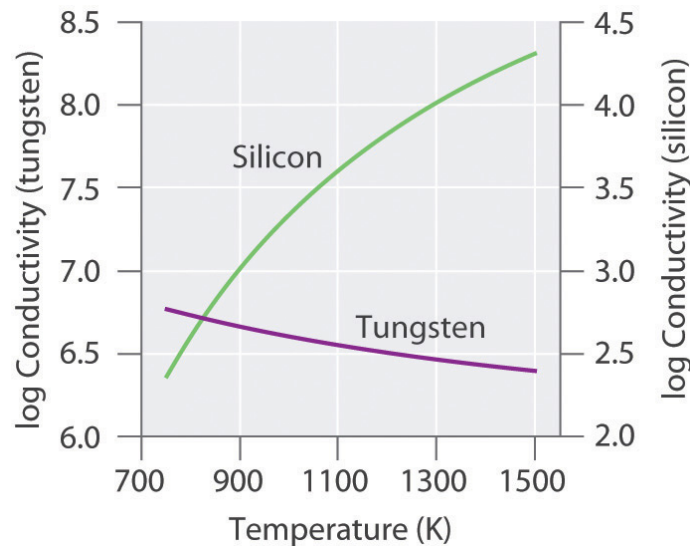

Figure 2.3 The conductivity of the semiconductor silicon and the metal tungsten as a function of temperature. The silicon increases conductivity with an increase in temperature while the tungsten shows an opposite trend in that the conductivity slightly decreases as the temperature is increased [9].

This heating-induced excitation in semiconductor devices can disrupt functionality through various mechanisms, and this is one reason devices have cooling apparatus to keep the semiconductors from getting too hot and ruining their effectiveness [10]. One can also use light to excite electrons from the valence band to the conduction band. If the wavelength of the light is adjusted so that the energy of the photon matches the bandgap energy, which is proportional to the wavelength, one electron per absorbed photon will be excited into the conduction band. If the wavelength is too long and thus energy too low, it will not have enough energy to excite an electron and the semiconductor will be transparent to the light. This is illustrated in Figure 2.4 where the UV/Vis transmission is shown for GaAs. When the wavelength of the light is below ~873 nm (1.42 eV) the energy is above the bandgap, and we see there is no transmittance because the light is being absorbed by the electrons and jumping the bandgap.
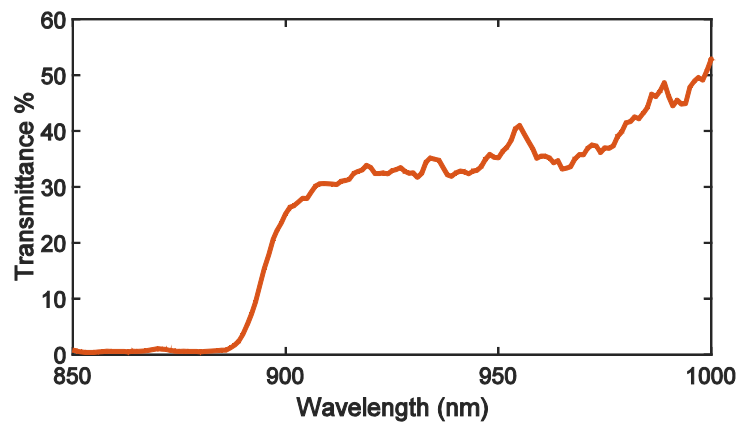
Figure 2.4 UV-VIS transmittance measurement of gallium arsenide. The transmittance increases dramatically at the bandgap corresponding to ≈873 nm or 1.42 eV for GaAs which is the reported value. As can be seen at the drop off the wavelengths that are longer or lower energy do not get absorbed while the shorter wavelengths which have higher energy are absorbed and excite electrons directly into the conduction band and thus the light is absorbed not transmitted.

As the wavelength of the light is increased above the bandgap we see a sharp increase in transmittance as the photons cannot energize electrons enough to make a direct transition from the valence band to the conduction band.

Many current semiconductor devices work dependent on another means of carrier excitation, namely by applying a voltage to the semiconductor to excite electrons into the conduction band. Typically, the two physical processes that are considered to lead to excitation of electrons into the conduction band due to an applied electric field are Zener tunneling (ZT) and impact ionization (IMI). Of the two processes, it is understood that IMI is responsible for the functionality of most semiconductor-based devices.
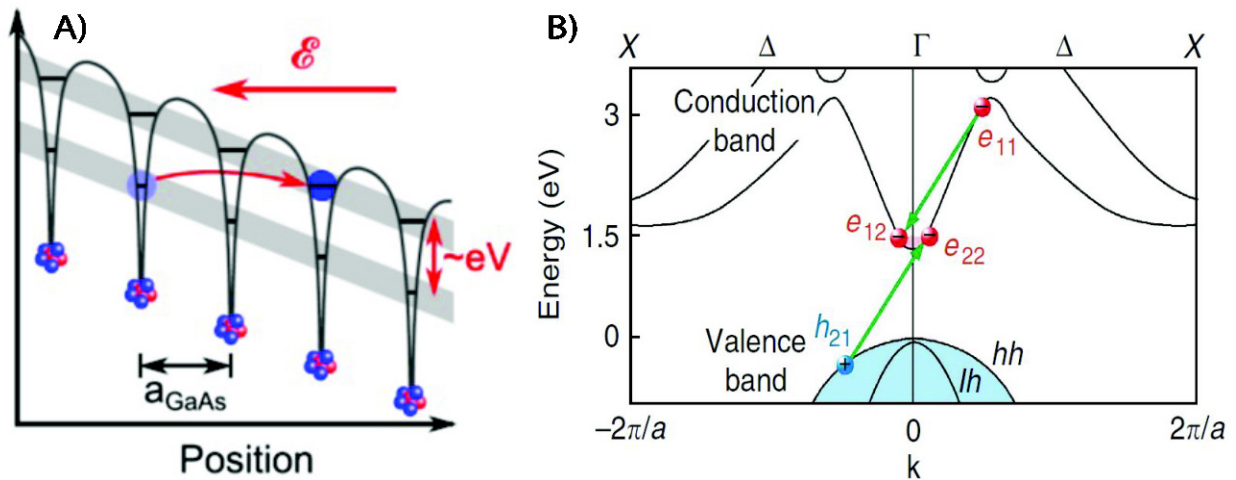
Figure 2.5 Two processes of electric field induced electron excitation. A) Depiction of Zener tunneling. An electric field is applied to the material thus contorting the conduction band and the valence band in such a way that electrons can tunnel across the lowered energy barrier. Adapted from Ref [11]. B) We see the process of impact ionization where one electron is accelerated up the conduction band colliding with a valence band electron thus we have two electrons in the conduction band. Adapted from Ref [12].

ZT is a phenomenon where an applied electric field causes a distortion of the electronic bands. In Figure 2.5A, we see a depiction of how ZT works. As an electrical field is applied to the

www.manaraa.com

medium, resulting in the distortion of the valence and conduction bands (gray lines depicted in 2.5A) in such a way that the potential energy wells and associated conduction band energy (illustrated by the unit cells, solid blacks lines, and upper thick grey line in 2.5A) will be lowered to be the same energy as the valence band at a different position in the crystal (indicated by filled blue circles and red connecting arrow in Figure 2.5A) [13]. This energy level manipulation allows electrons to subsequently tunnel from the valence band to the conduction band, increasing the conduction band population. ZT requires extremely high electric fields to become efficient.

Figure 2.5B depicts the IMI process in GaAs, showing how an electric field can accelerate an electron in the conduction band to high enough energies, such that if it collides with an electron in the valence band, energy transfer can result in exciting the valence band electron into the conduction band, leading to two electrons in the conduction band. This is depicted in Figure 2.5B the red dot labeled e_{11} is an electron that is already in the conduction band that has been excited by an electric field. This accelerated electron will collide with an electron in the valence band depicted as the blue h_{12} dot. The kinetic energy from the accelerated electron can be transferred to the valence band electron, resulting in two electrons in the low energy point of the conduction band. This process can begin again, now with twice as many electrons accelerated in the conduction band. On femtosecond timescales, this process can be cascaded multiple times, quickly increasing the number of conduction band electrons to exceedingly high carrier concentrations and radically increasing the electrical conductivity of the material [14].

There are times when ZT will be more relevant than IMI. An example would be when there are no carriers in the conduction band to begin. Although ZT is less efficient than IMI, it can create an initial carrier population of the conduction band. IMI is much more efficient than

ZT, but must have carriers in the conduction band to begin. Knowing these basic parameters of semiconductors is essential to our understanding of our research. In particular, the semiconductor behavior at THz frequencies.

The two main schools of thought for populating a conduction band at these frequencies are ZT and IMI. Both have been attributed with being the main contributor or carrier multiplication in semi-insulating GaAs, Fan *et. al.*[15] attributes this to IMI while Lange *et. al.*[11] promotes the ZT route. In our experiment, we investigate this discrepancy further to understand more clearly the behavior of semiconductor electrons at THz frequencies.

Chapter 3

Critical-Field Measurements of Gallium Arsenide at THz frequencies

The high frequency limit of electronic devices is constantly being extended, and the feasibility of components operating at even THz frequencies is being discussed more and more [16]. Many plausible THz electronics, including THz transistor electronics and THz high power amplifier modules [17], have the potential to be orders of magnitude faster than current devices, with the ability to also operate at higher temperatures, thus eliminating cooling needs and reducing energy usage [18]. Higher voltage operation can result in additional energy savings [19]. For such technological advancements to occur, a deeper understanding of how fundamental electronic processes can be controlled with ultrafast THz electric-fields is needed. At THz frequencies, material properties may not behave in the same way they do when subjected to lower frequency perturbations; indeed, nearly all material properties are frequency dependent [20].

For an example of central importance to a myriad of microelectronic devices, the critical electric field at which carrier multiplication is initiated increases with increasing frequency of an applied electric field [19]. This increase in critical field with frequency is a well-known phenomenon moving from DC to kHz and higher frequencies [21], but to date the frequency dependence of the critical field at THz frequencies has not been measured in any material. In this

chapter, we utilize extremely high-field THz radiation to measure the critical field in GaAs at frequencies from 0.7 to 1.5 THz.

We build on the influential papers of Fan *et al*. [15] and Lange *et al*.[11], where each showed THz induced carrier multiplication in doped and un-doped GaAs samples. The carrier multiplication in each case was initiated at only a single THz frequency, and due to atomically strong electric fields, exotic electronic effects such as field-induced degenerate electronic states could be observed [22]. Even though there were strong similarities in the experimental measurements of Fan *et al.* [15] and Lange *et al.* [11], different underlying routes to carrier multiplication were presented, with Fan focusing on IMI and Lange ascribing the results to ZT. By measuring the frequency dependence of the THz critical field, we can better understand the influence of ZT and IMI on the THz carrier multiplication. We also radiate GaAs, a promising material for use in many high-speed electronic devices [23], with high power THz radiation (>1 MV/cm peak-to-peak field strength). This strong electric field is locally enhanced by arrays of gold split ring resonator (SRR) metamaterial structures of varying sizes, which act as micro-LC circuits with corresponding resonant frequencies [24]. At the SRR resonant frequency, the THz electric field is significantly enhanced locally (~20×); an incident broadband THz pulse with a range of frequencies will have frequency specific field enhancement. We observe strong nonlinearities in intensity dependent THz transmission measurements through the GaAs metamaterial structures.

The critical electric field of a semiconductor is defined as the electrical breakdown or conduction point of a semiconductor. [25] The point of breakdown occurs when many electrons have been excited to the conduction band (carrier multiplication), significantly increasing the conductivity of the material. In semi-insulating GaAs, the critical field at zero frequency (DC

fields) is 320 kV/cm [26], and we expect this to increase with frequency as has been shown for many materials [19].

In the previous chapter, we discussed how two electric-field-induced processes, Zener tunneling (ZT) and impact ionization (IMI), can induce carrier multiplication. These two processes are the main contributors to the population of the conduction band when using electric fields. Therefore, having a good understanding of which process is influencing our semiconductor the most in the population of the conduction band is essential to the understanding of the critical fields at THz frequencies.

Intense single-cycle THz pulses were generated with an organic THz generation crystal OH1 via optical rectification [27] using 1450 nm light with pulse energies of ~0.9 mJ and pulse duration ~100 fs.
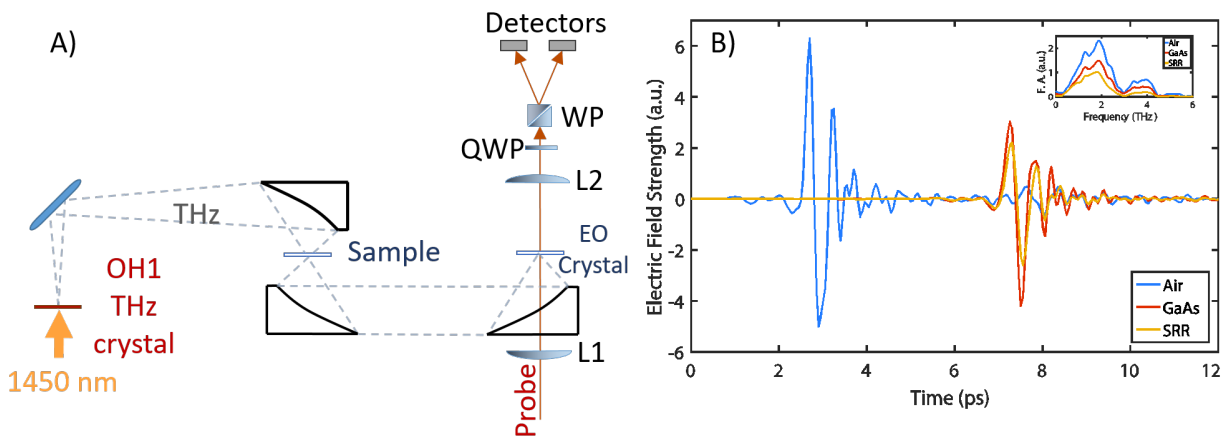

Figure 3.1: A) The THz transmission measurement setup. THz was generated with an OH1 generation crystal and directed to the sample. After passing through the sample it was directed to an EO crystal where the THz waveform could be recorded.
B) Transmitted traces are depicted from no sample, bare GaAs, and an SRR array deposited on GaAs. GaAs and SRR traces are delayed in time with respect to air due to the decreased group velocity in the samples relative to air. The amplitudes are smaller due to reflection from the surface and absorption within the sample. Inset: The FT of the three time traces shown. Note that in the SRR data a noticeable dip can be seen around 1.1 THz relative to the bare GaAs data.

19

First, the focused THz radiation was measured at the sample position using electro-optic sampling in 100 μm thick GaP crystal for a quantitative measurement of the time-dependent absolute field strength [28], showing peak-to-peak field strengths ranging from ~0.1 up to 1.2 MV/cm (Figure 3.1B). The main THz spectral intensity was in the range from approximately 0.3 THz to 3 THz (Figure 3.1B inset).

Gold SRR arrays of four different sizes (see Figure 3.2) were photolithographically deposited on a 500 μm thick sample of high-purity, semi-insulating GaAs. A photolithographic mask was made and patterned structures were deposited consisting of a ~50 nm of gold over a thin 9 nm layer of chromium that helps the gold adhere to the sample surface. Each SRR array was deposited over a 2 mm × 2 mm area. This sample preparation was performed by Tyler Westover, a graduate student in the lab of Professor Robert Davis in the department of Physics and Astronomy at BYU. SRRs with side lengths of 36, 28, 23, and 19.5 μm had corresponding resonant frequencies of 0.68, 0.95, 1.15, and 1.48 THz.

The THz was transmitted through the sample position and directed to a secondary position for electro-optic measurement of THz transients (Figure 3.1A). THz transmission measurements were recorded without a sample, with the THz directed through bare GaAs, and finally through each SRR array individually. The THz spot size is such that hundreds of SRRs within a given array are illuminated simultaneously. In all measurements, the THz power was controlled by rotating the first of two THz wire-grid polarizers. Time-domain THz transmission measurements were recorded on one SRR array at a time.
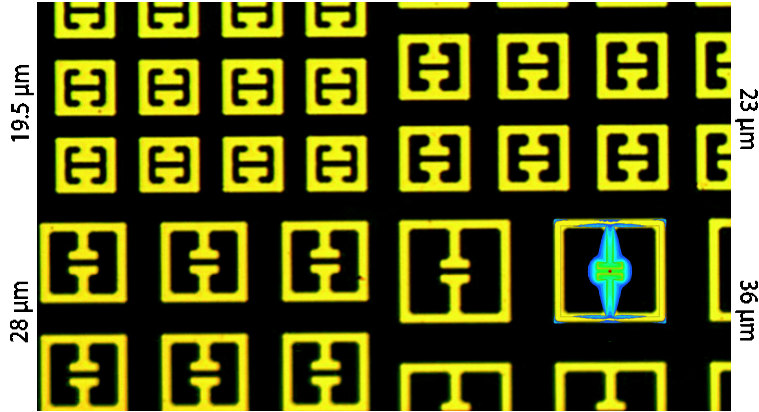
Figure 3.2: The intersection of the 4 SRR arrays deposited on semi-insulating GaAs. Each SRR array is 2 mm x 2 mm. The label next to each section indicates the width, and resonant frequency of each square SRR in the associated array. The highlighted SRR in the 36 μm array is showing the calculated enhancement with ~20× enhancement of the electric field in the capacitive gap.

Power dependent traces were collected by varying the THz electric field strength by rotating the first of two wire grid polarizers. For all the traces shown in Figure 3.3, the real part of the transmission coefficient (transmission) is calculated as the ratio of the spectral amplitude of the THz transmitted through an SRR array, divided by the spectral amplitude of the THz transmitted through bare GaAs. For the largest SRR data shown (36 μm width), the resonant frequency is the lowest at 0.68 THz. As the SRR size is reduced to 28 μm and then down to 23 μm, and finally to 19.5 μm the resonant frequencies increase to 0.95 THz, 1.15 THz and 1.48 THz respectively.

Interesting trends are found in these measurements. First, as the THz electric field is increased, the transmission minimum in the dip also increases. Second, the resonant frequency shifts to slightly lower values as the minimum transmission amplitude increases with increasing incident THz field strength (Figure 3.4).
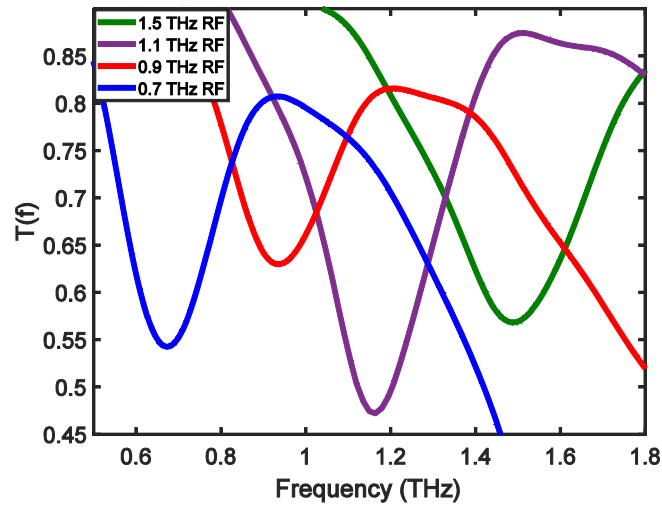
Figure 3.3: Resonant frequency transmission for each SRR array. A noticeable dip in each trace is evident at the SRR resonant frequency. Each trace here was recorded at low incident field strength.

The increase in transmission at the resonant frequency comes as a result of an increase in the number of free carriers in the conduction band [15,12]. The free carriers are generated locally in the GaAs close to the capacitive gap where the electric field is locally enhanced, and not in the rest of the bulk GaAs sample. At low THz power the GaAs acts as an insulator, allowing the LC circuit to function properly and absorb at the resonant frequency. As the THz electric field is increased, carrier multiplication sets in and the number of carriers (and conductivity) increase significantly, allowing electrons to flow across the capacitive gap, shorting out the LC circuit and diminishing the LC resonance.
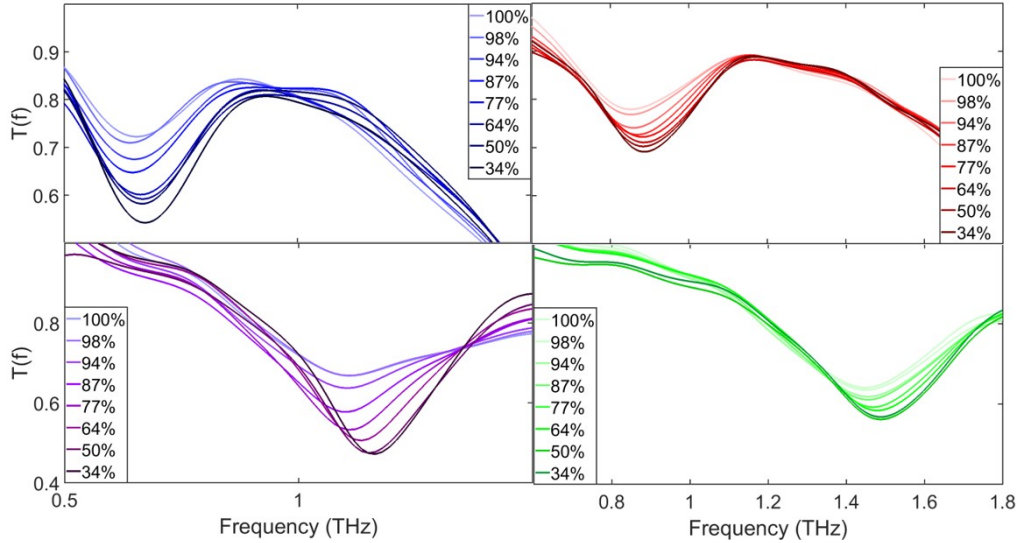
Figure 3.4: Power dependences of each SRR array. At low power the resonant dip is prominent because the GaAs in the capacitive gap is insulating, as the power is increased the GaAs becomes more conducting. This effect shorts out the SRR and the dip diminishes.

The minimum in transmission at the SRR resonance is plotted against the THz electric field strength at the sample position (Figure 3.5A), and in each we see unique, nonlinear increases in transmission as the THz electric field strength is increased. Figure 3.5B shows the transmission normalized to the low field value, allowing easier direct comparison between the SRR arrays. Each normalized, power dependent set of SRR data was fitted to a 2nd order polynomial, and from the fit interpolation we identified at which THz field strength the transmission increases by one percent, thus allowing us to approximate when carrier multiplication begins. We chose this electric field value as the critical field at the frequency of the SRR resonance as this relates to the change in transmission that has been related to the carrier density for a critical field value.

23
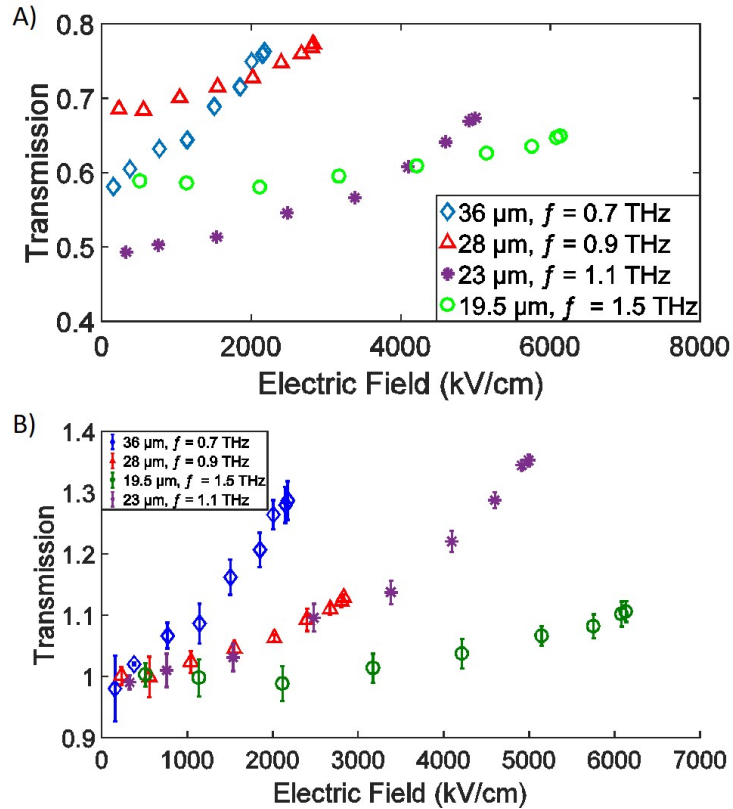
Figure 3.5: Measured transmission amplitude at the resonant frequency compared with the enhanced electric field strength in the capacitive gap A) and normalized B). Note that the SRRs transmissions increase at different rates. The higher frequency SRRs need higher field strengths to have the same increase in transmission.

The green triangles in Figure 3.6 show the critical field as a function of frequency, with the blue triangle the DC critical field value from the literature [26], and we see a strong frequency dependent increase to the critical electric field from 320 kV/cm at DC fields to 2300 kV/cm at 1.5 THz.

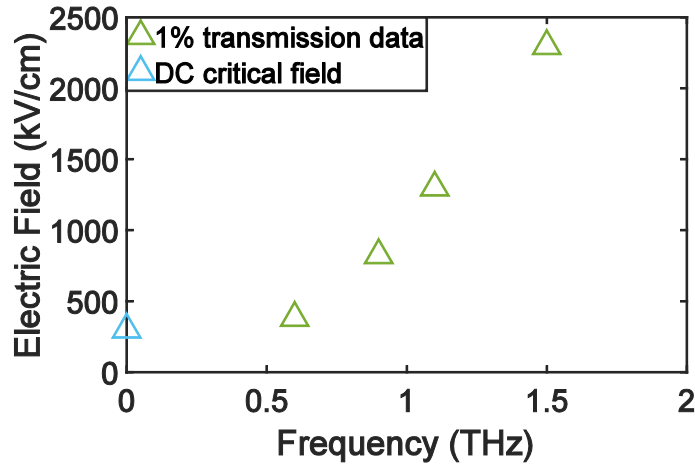Figure 3.6 The critical fields for the frequencies 0.7, 0.9, 1.1, and 1.5 THz are shown. The reported DC critical field of 320 kV/cm is shown as the blue triangle at zero frequency [26].

To better understand the THz frequency dependence of the critical field, we attempt to model the local SRR electric field enhancement and the subsequent carrier dynamics according to equations governing ZT and IMI. The THz electric field does not have sufficient energy to excite the carriers directly. The bandgap of GaAs is 1.42 eV [29], while the photon energy of 1 THz is only 4.1 meV. Fan [15] and Lange [11] reported similar increases in nonlinear transmission through meta-material SRR layers on GaAs; as mentioned above, Fan *et al.* attributed this to impact ionization [15], whereas Lange *et al.* concluded it resulted from Zener tunneling [11]. Regardless of the method, both ZT and IMI require strong electric fields to initiate these processes. We used SRR structures to locally enhance our already strong fields, and calculations of the electric field enhancement are shown in Figure 3.7.

THz frequency electric field enhancement in the capacitive gap of the SRR structures was calculated using HFSS modeling; these calculations were performed by Junming Diao, a graduate student in the lab of Professor Karl Warnick of the Department of Electrical and Computer Engineering at BYU. The frequency-dependent, calculated SRR enhancement at the

25

center of the capacitive gap is shown in Figure 3.7A for each of the four SRRs; the structures were found to enhance a range of frequencies centered around the designated resonant frequency to ~20× the incident field strength. The electric field is enhanced locally in the capacitive gap and not in the bulk of the GaAs sample (see Figure 3.2 highlighted SRR). As such, carrier multiplication would occur only in the GaAs where the local field enhancement occurs, and the majority of the sample remains unchanged.
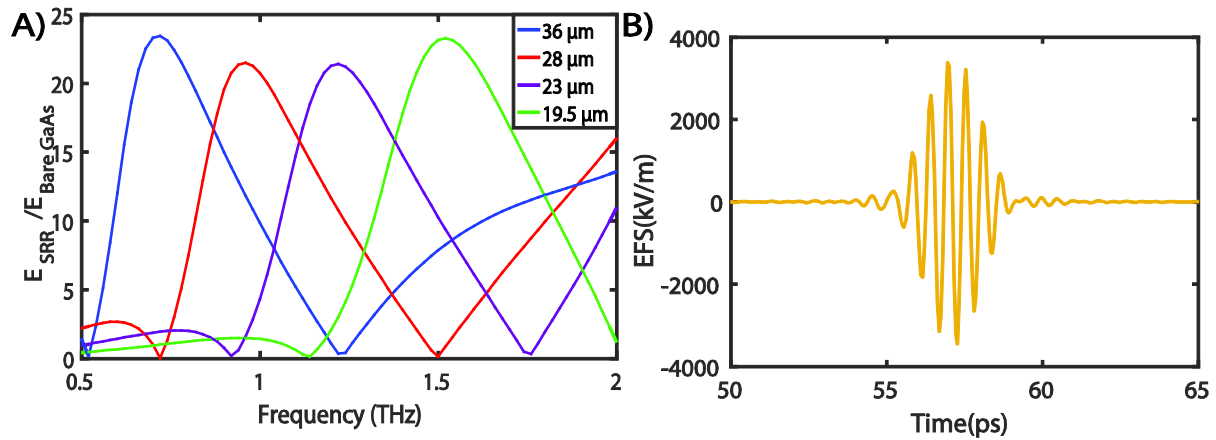

Figure 3.7: A) Calculated electric field enhancement for SRR structures. Each structure enhanced a range of frequencies centered around the resonant frequency. The structures each display a similar enhancement of the resonant frequency of around 20×. B) The calculated enhanced electric field for the 1.5 THz enhancement structure. This was calculated by multiplying the enhancement factor to the Fourier transform of the original electric field trace then inverse Fourier transforming the product of the two.

To calculate the actual electric field produced by the enhancement of the SRRs, we performed a Fourier transform on the electric field trace measured at the sample position and then multiplied this by the enhancement factor from Figure 3.7A giving us the enhanced electric field in the frequency domain. An inverse Fourier transform back to the time domain shows the frequency-specific enhanced electric field produced in the gaps of the SRRs (see Figure 3.7B for the 1.5THz SRR). This enhanced electric field was used for the peak electric field strengths for

26

the x-axis in Figures 3.5A and B above and therefore to calculate the critical field in Figure 3.6. The enhanced electric fields were also used in the carrier dynamics analysis that follows.

By measuring the frequency-dependence of the critical field and modeling the frequency-dependence of the carrier dynamics, we attempt to shed light on the discrepancy between Lange *et. al.* [11] promoting the ZT model and Fan *et. al* [15] supporting an IMI model. The GaAs sample is semi-insulating, and as a result the initial number of carriers in the conduction band is low in comparison to a conductor (approximately 1.79×10^6 cm^{-3} at room temperature [12]). Because the carrier density is low, Lange *et al.* assumed that ZT was the predominate route to carrier multiplication. In the ZT picture, as the THz electric field interacts with the sample it acts to bias the crystal lattice, allowing tunneling from the valence band into the conduction band spatially, and therefore ZT could act to initially populate an empty conduction band. On the other hand, the conduction band is not vacant of electrons at room temperature, and the THz electric field could directly accelerate these carriers, allowing IMI cascades to initiate and increasing the conductivity. The enhanced THz transient occurs on picosecond timescales (see Figure 3.7B) and several occurrences of IMI can occur within this short time frame [12].

The Zener tunneling model allows us to predict the rate at which electrons can tunnel into the conduction band, as a function of the applied electric bias field. Equation 3.1 gives the tunneling rate r_z as [11]

$$r_z = \frac{e^2 \varepsilon_n^2 m_r^{1/2}}{18\pi\hbar^2 E_g^{1/2}} \exp\left(\frac{-\pi m_r^{\frac{1}{2}} E_g^{\frac{3}{2}}}{2\hbar e \varepsilon_n}\right), \qquad \text{Eq 3.1}$$

where $\mathcal{E}_n$ is the applied electric field, E_g is the band gap of GaAs, m_r is the relative mass of the electrons, e is the electron charge, and $\hbar$ is Planck's constant. The tunneling rate shows us the

27

rate at which electrons can tunnel when an electric field is applied to them. In Figure 3.8A, we see the tunneling rate as a function of time with the enhanced, time-dependent electric field as input, where each line is calculated from different electric field strengths. The tunneling rate can be directly inserted into a differential equation to solve for the carrier density as a function of time (see Figure 3.8B). At the end of the THz pulse, the carrier density reaches a maximum, and the maximum is graphed as a function of electric field below in Figure 3.10A. We note that there is some frequency dependence in the ZT as the different frequency lines separate at higher electric field   percentage, but as we will see, in comparison to the IMI, the ZT frequency dependence is weak (see Figure 3.11).
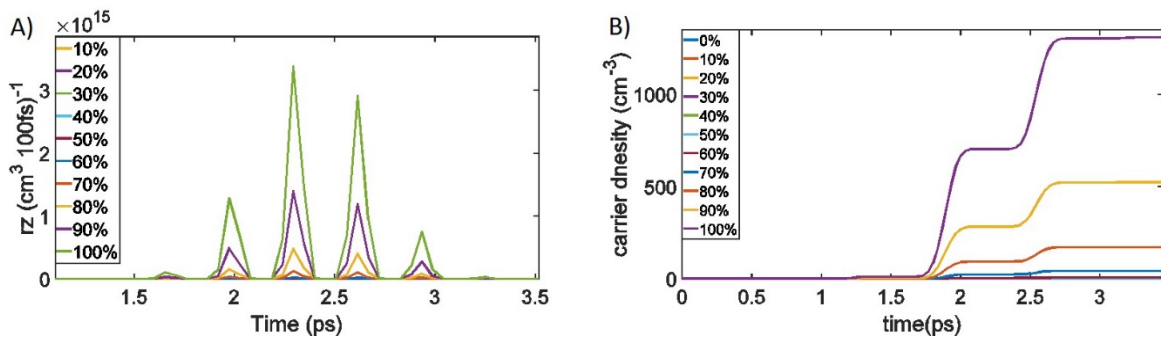
Figure 3.8 A) The tunneling rate at various electric field strengths (10-100%). This shows that the rate goes up in the peaks of the THz waveform. B) This is a plot of the solved rate equation showing the carrier density as a function of time. Each line is also an electric field strength from 0% of the max to 100% of the max.

There are two main ways IMI is explained in the literature [12, 15]: in terms of acceleration of conduction band electrons in wavevector space [12], or by accelerating the electrons in real space to a velocity where the kinetic energy is high enough to collisionally excite valence band electrons [15]. In reality, the two descriptions are identical, but there are

some mathematical simplifications used in explaining each, which influence the predicted carrier dynamics.

In the wavevector space picture, as the electron is accelerated along the GaAs conduction band in the (100) direction, it can reach a wavevector magnitude with energy equal to or exceeding the bandgap energy [12]. Equation 3.2 below describes how, according to Bloch-theory, the wavevector k changes in time as the electrons are accelerated by an electric field $\mathcal{E}(t)$. Equation 3.3 is the same equation as Equation 3.2, but now emphasizing the velocity picture and including the addition of the relaxation term due to carrier scattering that can reduce the velocity [12], [15].

$$\hbar \frac{dk(t)}{dt} = -e\mathcal{E}(t) \qquad \text{Eq. 3.2}$$

$$\frac{d\langle v(t)\rangle}{dt} = \frac{e\mathcal{E}(t)}{m_e} - \frac{\langle v(t)\rangle}{\tau(\mathcal{E})} \qquad \text{Eq. 3.3}$$

Eq. 3.3 accounts for carrier-carrier scattering with the second term on the right, where τ is the mean scattering time, $\langle v(t)\rangle$ is the average electron velocity, $\mathcal{E}(t)$ is the enhanced THz electric field, e is the charge on an electron, and m_e is the relative mass of the electron. In equation 3.2 $k(t)$ is the wavevector, $\mathcal{E}(t)$ is the applied electric field, e is the charge of an electron and $\hbar$ is Planck's constant divided by 2π.

Using Eq. 3.2, we determined when IMI events occur by calculating when the wavevector magnitude exceeds the threshold value corresponding to an energy as large as the GaAs bandgap. The threshold wavevector was calculated according to the band structure to be $\pm 3.43 \times 10^9$ m^{-1} [14, 30]. Figure 3.9A shows the electron wavevector time-dependence; each time

29

the wavevector reaches the threshold an IMI event occurs and the electron returns

instantaneously to a zero wavevector (according to the simplified model), and can then be

accelerated again. Each time an IMI event takes place, the number of carriers in the conduction

band doubles. Once we have determined how many IMI events are caused by the electric field,

and at what times they occur, we use Eq. 3.4 to model the increase in carriers in time, as shown

in Figure 3.9B [12].

$$C = N_0 * 2^{n_i}$$
<div align="right">Eq. 3.4</div>

Where C is the total carrier concentration, N_0 is the initial carrier concentration, and n_i is the IMI-
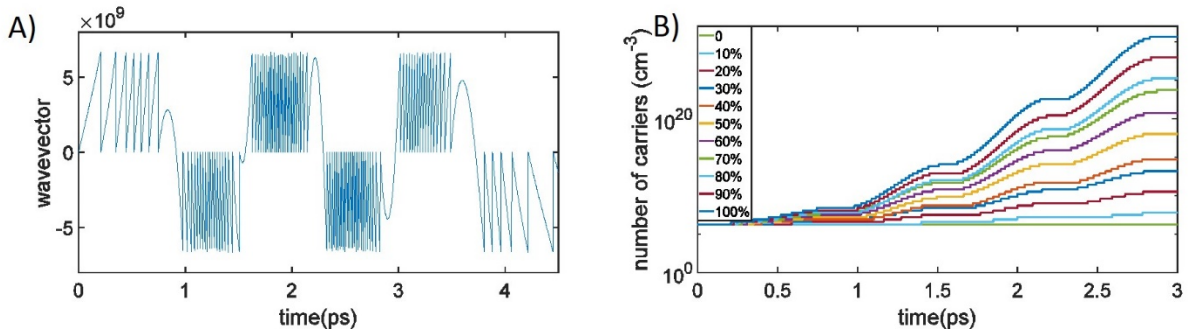
event number calculated from Equation 3.2.

Figure 3.9 A) Wavevector movement for electrons in the conduction band as a function of time as the electric field accelerates the electron. When an electron reaches the threshold wavevector magnitude, and IMI event occurs and resets the wavevector back to zero. B) The carrier density as a function of time with each line representing different electric field magnitudes.

As we did with the ZT modeling, we plot the max carrier concentration as a function of

the electric field as a function of peak electric field from the data in Figure 3.9B, and plot this in

Figure 3.10B. The modeling process is done as a function of frequency, giving the various lines

we see on Figure 3.10B. The max carrier concentration varies with the frequency of the applied

www.manaraa.com

electric field; to reach a given carrier concentration, a higher electric field is needed as frequency increases. Due to some simplifications in the model, the max carrier concentration in Figure 3.10B exceeds a feasible value. Because we are only interested in the frequency dependence of the critical electric field at which carrier multiplication initially increases (and also where the model approximations should be more reasonable), we can extract the frequency dependence at these initial concentrations. Therefore, we choose a carrier concentration that relates to our observed 1% transmission change according to modeling of the conductivity [11], to determine the frequency dependence of this model. The frequency dependence for the wavevector IMI model is shown as the green line in Figure 3.11.

The wavevector dependent electron acceleration model of Equation 3.2 was used to describe electron acceleration along the conduction band, but it neglects carrier scattering that will disrupt this acceleration, and restricts the carriers to only one of many conduction bands. Equation 3.3 is a simple model for how the average electron velocity $<v(t)>$ increases as electrons are accelerated by an electric field $\mathcal{E}(t)$, and includes (in the second term on the right) a mean velocity relaxation time to account for carrier scattering. We insert model oscillating electric fields of varying frequencies and solve the equation for each frequency, giving a time dependent $<v(t)>$. Figure 3.10C below shows the model results for 2 input frequencies; the solid lines are input electric fields of equal amplitudes and frequencies of 0.7 and 1.5 THz (representative of our lowest and highest frequency SRRs). The dashed lines are the average electron velocities for each frequency. We can see that for equivalent electric field strengths, the electrons are accelerated less for the higher frequency. As an electric field interacts with a material, it serves to accelerate the electrons in the material. As the sign of the oscillating field flips, the direction of acceleration changes. When fields of higher frequencies are used, this flip

31

in direction happens faster allowing less time for the electrons to accelerate. Thus, to reach the

same average velocity of a lower frequency electric field, higher field strengths are required to

allow electrons to reach the same velocity at higher frequencies, resulting in an increase in

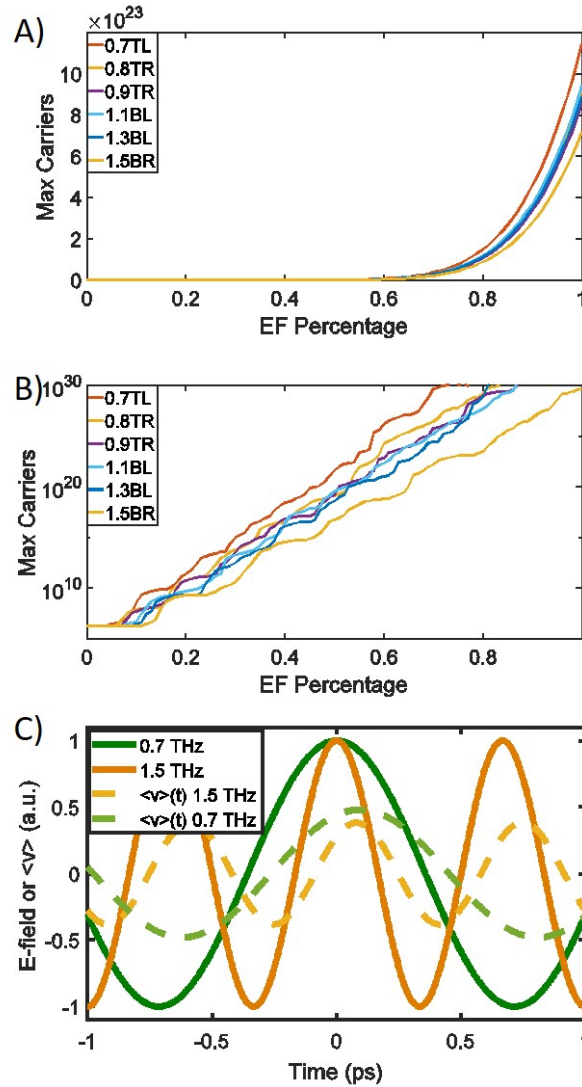critical field strength as a function of frequency.

Figure 3.10: Comparison of the frequency dependence in increasing carriers in the conduction
band of the GaAs with A) Zener tunneling Eq. 3.1 and B) IMI modeled from Eq. 3.2 and 3.4 C)
Eq. 3.3 shows the how the velocity of the electron changes with the changing of the frequency of
the THz field.

In Figure 3.11 we plot the results of our modeled critical field strengths in comparison to our experimental data. The red, orange, and purple lines are from the velocity IMI model just discussed (Eq. 3.3). Each line is calculated using a different carrier scattering time τ. Longer relaxation times result in an increased critical electric field required for electrons to reach threshold velocity, and in each case the critical field increases with the frequency of the driving field. The blue line is the frequency dependent critical field extracted from ZT modeling in Figure 3.10A. There is an increase in critical field with frequency according to the ZT model, but it is weak in comparison to the experimental results.
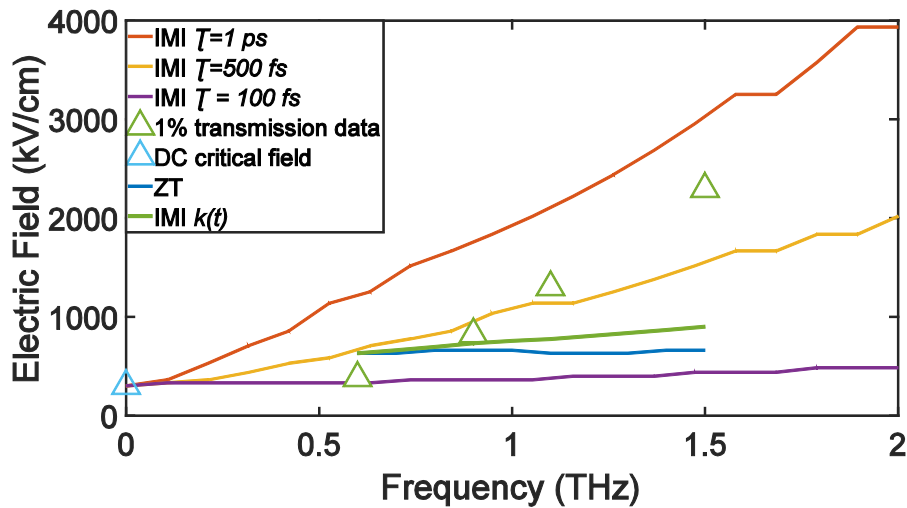
Figure 3.11: The critical electric field as a function of frequency in GaAs. Green triangles are the electric field strength needed to produce a 1% increase in the transmission. The blue triangle is the critical field value for a DC field [26]. Solid lines are the calculated critical field according to IMI and ZT modeling. IMI model predictions from Eq. 3.3 are shown as red, orange, and purple lines where the scattering time τ was respectively 1 ps, 500 fs, or 100 fs. IMI model predictions from Eq. 3.2 and 3.4 is shown as the green solid line. The blue line is the model for frequency dependence for ZT.

In comparing the models to the actual data, it appears that IMI modeling better represents the observed frequency dependent critical field. In reality, likely a mix of ZT and IMI are

www.manaraa.com

occurring in the sample. ZT could help initially increase the carrier concentration, but then IMI quickly takes over in a way that gives the observed frequency dependence. The modeling helps support the importance of IMI in the carrier multiplication process at THz frequencies and ultrafast timescales.

To conclude, we measured the frequency dependence in the critical field at THz frequencies (a first for any material). We report a critical field in semi-insulating GaAs as 400 kV/cm, 800kV/cm, 1300kV/cm, and 2300 kV/cm for the frequencies of 0.7, 0.9, 1.1, 1.5 THz respectively. The observed increase in critical field with frequency leads us to conclude that although Zener tunneling might initially help small numbers of carriers populate the conduction band in the GaAs, but the major contributor to carrier multiplication at THz frequencies, and the reason for the observed frequency dependence, is impact ionization. These results are crucial to the design of high-speed electronic devices that could operate based on THz frequency electric field induced carrier multiplication as the critical field at which semiconductors switch is needed to design the transistors in the processor.

In future experiments, we will seek to broaden the range of frequency dependent measurements through broadband local electric field enhancement with fractal antenna structures (which also offer larger theoretical enhancement than the SRRs). Temperature-dependent experiments and pump-probe measurements will also help reveal the intricacies of excited carrier dynamics and relaxation (what happens after the THz excites the carriers into the conduction band).

Chapter 4

Introduction to Single-Shot Measurements

In a classic ultrafast pump-probe measurement, probe pulses must be stepped in time to map out the signal, one relative pump-probe delay at a time. Often many shots are recorded at each step to average for noise reduction. In Figure 4.1 we see a THz transient that was recorded from the setup shown previously in Figure 1.2. Each circle in Figure 4.1 corresponds to a translation-stage position, where the stage with a retroreflector would move, stop, and record a set amount of pulses to average; then the stage would move to the next step and repeat with the distance between points determining the sampling rate. These classic pump-probe measurements have some disadvantages, which include the time it takes to record, potentially from minutes to hours depending on the speed of the stage and the number of stage positions (often 300 points for many of our measurements). A scan length is ultimately determined by the constraints of the experiment: how long a time window data needs to be collected over and what time step is needed for appropriate signal sampling. Signal-to-noise considerations may necessitate long averaging times (many measurements per stage-position). For many of our measurements, as few as 150 measurements per stage position is adequate.
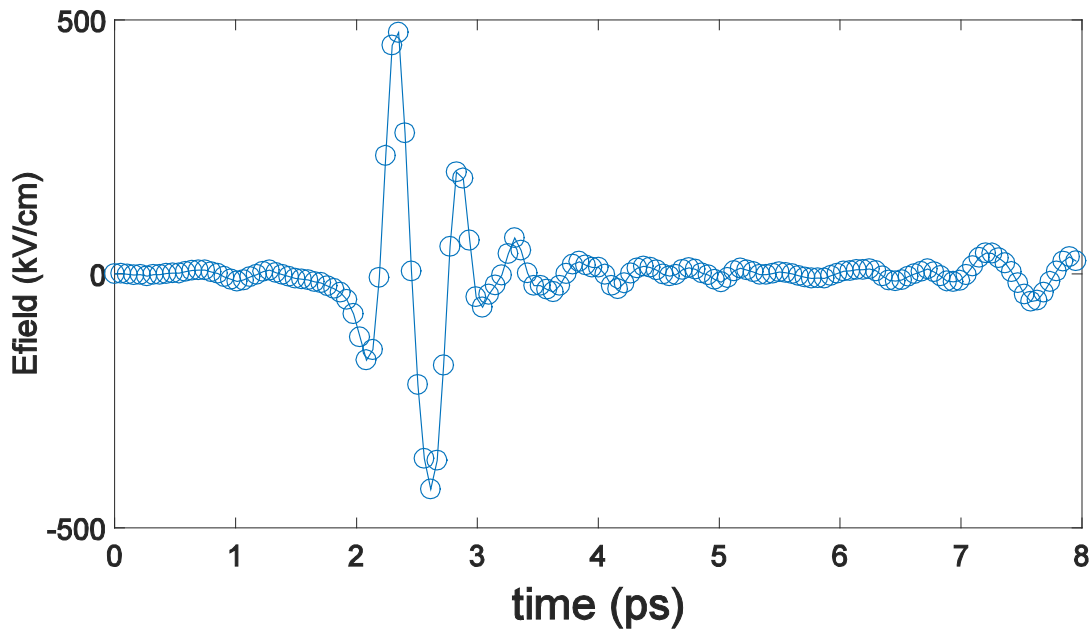
Figure 4.1 This is a THz waveform recorded using a classic pump-probe EO sampling technique. Each circle is recorded for a specific stage position, averaging ~150 measurements.

New research advancing the world of ultrafast spectroscopy is known as single-shot spectroscopy [31-33]. There are multiple ways that single-shot spectroscopy can be performed [32-34], and we have developed a new scheme for single-shot measurements based on spectral encoding. In this chapter, we give an overview of our innovative technique. The main premise behind spectral encoding is that a short laser pulse can be stretched (chirped) in time such that frequencies are spread out temporally. Probing with such a chirped pulse allows the signal to be encoded onto the probe pulse spectrum (Figure 4.2). Using single-shot probing, an entire trace such as the THz trace shown in Figure 4.1 can be recorded nearly instantaneously. In addition, to reducing measurement time, single-shot probing techniques allow us to record destructive processes; traditional pump-probe processes require repetitive events. Destructive processes leave the sample damaged once they have been exposed to the light, and therefore a single probe

shot is required to capture the dynamics, which would be impossible to do with hundreds of

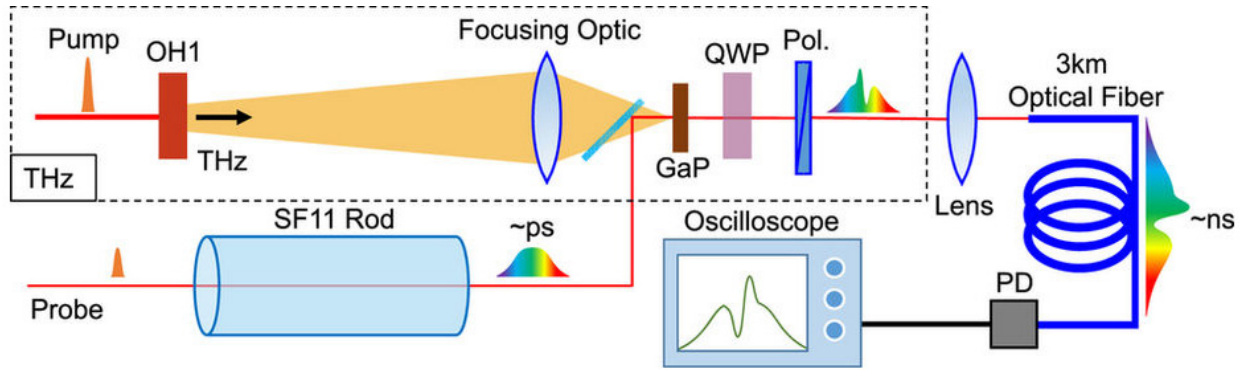pulses per stage position in classic pump-probe measurements.

Figure 4.2: A diagram of how a single-shot probing measurement works. GaP is an electro-optic crystal used for THz detection, QWP is a $\lambda/4$-waveplate, Pol. is a polarizer, and PD is a fast photodiode. Probe pulses are pre-stretched to picosecond timescales by passing through the SF11 glass rod, then they pass through the sample where the signal is encoded on the probe pulse. The picosecond probe pulse is then stretched to nanosecond time-scales by propagating through a 3 km long optical fiber, and the response from the sample and pump interaction is read out by a detector and recorded on a high-bandwidth oscilloscope. This diagram was adapted from our work published in [35].

We exploit the Heisenberg uncertainty principle to our advantage in this experiment. The

laser pulses are so short in duration (<1 ps) that the energy (proportional to frequency) is not well

defined. Therefore, there is a range of frequencies (and corresponding wavelengths) that make

up ultrafast pulses of light. A model spectrum for a 35-fs laser pulse is shown in Figure 4.3B. For

a ~100-fs laser pulse from a Ti:Sapphire laser like our own, the spectral FWHM is approximately

10 nm, with the spectrum centered at 800 nm. The dispersive properties of light in a medium can

be used to chirp a pulse from fs to ps time scales. As shown in Figure 4.3A for SF11 glass, the

refractive index of light is different for different wavelengths. For a normal dispersive material

that means that longer wavelengths will have a lower refractive index and therefore travel faster

in the medium, while the shorter wavelengths will have a higher refractive index and travel more slowly (see the labels in Fig. 4.3B). Thus, putting light through a medium like the SF11 rod displayed in Fig. 4.2, the pulse will be chirped in time with longer wavelengths at the pulse front and shorter wavelengths at the tail of the stretched pulse. In the optical-fiber based single-shot technique displayed in Fig.4.2, we use this pulse stretching technique twice. Once as pre-chirp, through an SF11 glass rod, and once as a post chirp, through a fiber optic cable. Since our measurements are a spectral encoding technique, the broader the spectrum of the pulse, the larger the time window we can record in a single pulse.

The pre-chirp part of the setup uses an 800 nm centered, 100 fs pulse of light from our Ti:Sapphire laser system. This light is directed through an SF11 glass rod which stretches our pulse to ~2 picoseconds (see Figure 4.2). This gives us a temporal window over which we can probe and map the time information. After the pre-stretched probe pulse passes through the sample and the dynamics are imprinted on the probe, we utilize the large dispersion of a 3-kilometer long fiber optic cable to stretch this encoded probe pulse out to the nanosecond time scale. Nanosecond waveforms are now on time scales that electronics in the form of a fast photodiode and oscilloscope can detect and record. Essentially, the dispersion in the fiber stretches the pulse in such a way that the spectrum is read out as a function of time. The oscilloscope has a 4 GHz max bandwidth meaning that it can record this nanosecond stretched pulse quite easily. The pump line in Figure 4.2 is a THz pulse produced in a similar manner to what is described more completely in Chapter 1. This THz pulse is directed to the sample and focused to line up with the probe in both space and time.
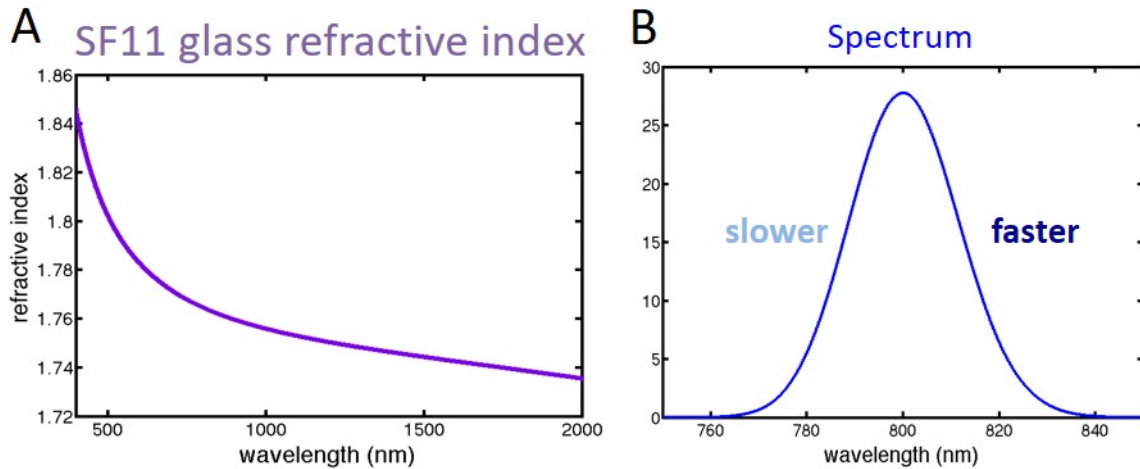
Figure 4.3: A) The refractive index for the SF11 rod used in our experiment as a function of wavelength. B) The spectrum of a 35 fs pulse centered at 800 nm. In a medium like SF11, the longer wavelength light will travel faster and the shorter wavelength light will travel slower, resulting in a stretched pulse.

It takes time to measure THz waveforms (up to many hours), and so one of our first demonstrations of the single shot technique was to record THz waveforms. Broadband THz radiation is generated via optical rectification of 1200 nm light in the organic THz generation crystal OH1(see Figure 4.2), in which the water vapor absorption and the OH1 phonons imprint modulations in the generated terahertz waveforms. Note that the focusing optic shown in Figure 4.2 was in practice a 90° off-axis parabolic reflector. The generated THz radiation is detected using an electro-optic sampling method. Figure 4.4A illustrates the observed output pulse-profiles from the photodiode with and without terahertz pulses, for different relative delay times between the terahertz pulse and probe pulse. We clearly see the difference of the waveforms induced by the terahertz pulses. By normalizing the terahertz signal by a reference probe pulse (grey lines in Figure 4.4A), $\Delta I(t)/I(t)$, the THz waveform can readily be compared to that recorded with a conventional stage scan method (the dark line in Figure 4.4B, recorded

www.manaraa.com

by stepping a delay stage to change the relative delay between THz and a ~100 fs 1200 nm
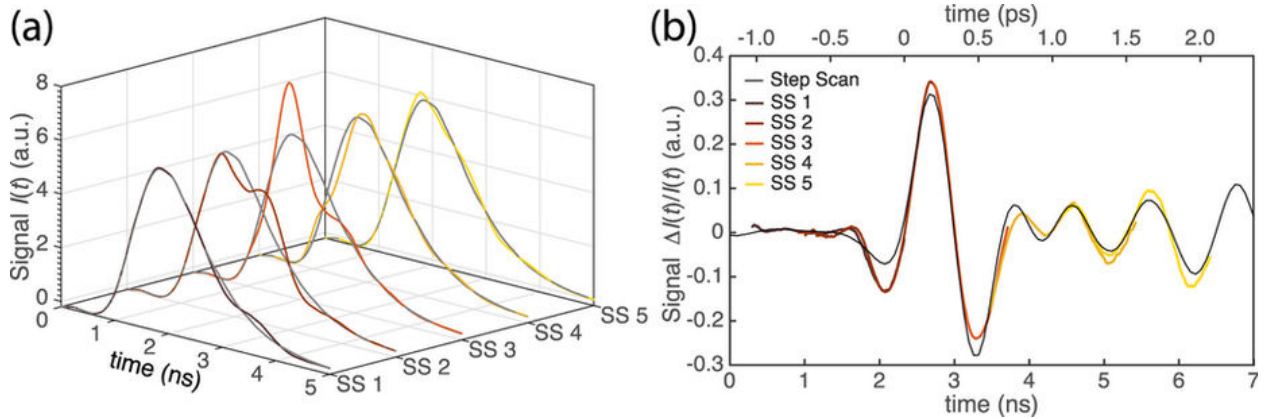
probe pulse).

Figure 4.4: (**a**) The probe profiles with and without the terahertz waves as the relative delay between THz and probe pulses was changed. (**b**) THz time traces compared to the step scan method. The black line indicates the time traces captured using the traditional step-scan method. The data with five different relative delay times are shown to demonstrate the precise measurement of the terahertz waveforms (adapted from our work in [35]).

In order to test the signal reconstruction and to calibrate the time-scaling factor, we

stepped the relative delay, increasing the relative path-length by a known amount, between the

pre-stretched probe and THz pulses and recorded scans at 5 different positions (labeled SS 1–

5 in Figure 4.4). The good agreement of these waveforms shows the effectiveness of the

simple calibration method and demonstrates the promising capability of this fiber single-shot

technique to record complex THz waveforms, potentially at exceedingly high acquisition

rates. Additionally, the ability to observe the complete THz waveform in real time allows for

easy optimization of experimental alignment.

40

In summary, we demonstrated novel single-shot high-repetition-rate measurements of ultrafast and terahertz waveforms by only using a long optical fiber, a single photodiode, and an oscilloscope. In Ref. [35], we realized the fast acquisition of THz transients, and additionally demonstrated recording Kerr waveforms in $LiNbO_3$ and an irreversible ultrafast phase change in a GST thin film. Our collaborators at the Yokohama National University performed the measurements on $LiNbO_3$ and GST, while the THz measurements were performed in our lab at BYU. Future work will aim to increase the temporal window of the single-shot detection, as well as to improve the time resolution, which will further enhance the variety of applications using this fast, simple, single-shot measurement scheme, for example, in fundamental sciences of irreversible and dynamic phenomena, terahertz imaging, information and communication technologies, material characterization, and so on. In the following chapter, we directly compare the fiber-based spectral encoding to a spectrometer-based measurement. We also comment on various corrections that may need to be performed to accurately recover the material response.

Chapter 5

Spectrally Encoded Single-Shot Probing with an Optical Fiber versus a Spectrometer

Single-shot spectroscopy is becoming a useful technique in the ultrafast community. As we have already developed a method for recording THz and other ultrafast transients in our previous work [35], we want to develop our understanding of the new single shot technique that can improve the accuracy of data extraction. To this end, we will here evaluate and compare two applications of spectrally-encoded single-shot spectroscopy to traditional pump-probe measurements.

We construct a simple 800 nm pump-800nm probe measurement to observe excited carriers in a 300μm thick GaP sample crystal. The probe pulse is chirped using two mechanisms so that the amount of stretching can be varied. We used an SF11 rod as described in the previous chapter, as well as a grating-based compressor within the laser. Using the compressor, we could provide positive or negative chirp such that the combination of compressor and SF11 rod resulted in a pulse ranging from the Fourier transform limited 100 fs stretched out to ~10 ps; the SF11 rod always had the same stretching effect, but we used compressor to vary the length of the pulse. This pre-stretched probe pulse was used to detect

42

the signal, and then the spectral-encoding signal was measured with both the spectrometer and the fiber + oscilloscope.

A traditional pump-probe measurement (shown below in Figure 5.2) reveals a fast reduction in transmission (the intensity of the transmitted probe on the detectors) due to 800 nm pump-excited carriers that creates a plasma in the sample. The plasma absorbs and reflects the probe light, but due to carrier relaxation, the signal quickly recovers. We measure the transient transmission in three ways (two of them simultaneously). First, we direct part of the probe light to a 3 km long fiber optic cable optimized for 800 nm and this light is stretched out to the nanosecond time scale by dispersion in the fiber. As shown in Figure 5.1A, this nanosecond pulse then can easily be read by our fast photodiode with a fast amplifier connected to the oscilloscope. We record traces with the pump blocked (purple line) and unblocked (blue line). The unblocked signal shows the nanosecond intensity profile of the pulse. In the pumped signal, we see a clear drop in intensity due to photo-excited carriers. Second, the other part of the probe beam is directed to a spectrometer. This USB2000+XR spectrometer by Ocean Optics covers the 200-1100nm range, has 2048 pixels, an optical resolution of 0.1 nm FWHM, and it is relatively inexpensive ($3000 versus ~$30,000 for the fiber, photodiode, amplifier, oscilloscope combo).

The spectrum is read out with this spectrometer which shows the same basic shape and features as the fiber data (see Figure 5.1B for the spectrometer pumped and unpumped signals). In the case of both the fiber and spectrometer measurements, the signal is constructed by subtracting the unpumped signal from the pumped signal (ΔI), and then normalizing it by the unpumped signal (I_0) to give $\Delta I/I_0$ shown in Figures 5.1C and D. In

these Figures 5.1C and D we have plotted the signal for different compressor settings, resulting in different pre-stretched pulse durations and corresponding probe time-windows.
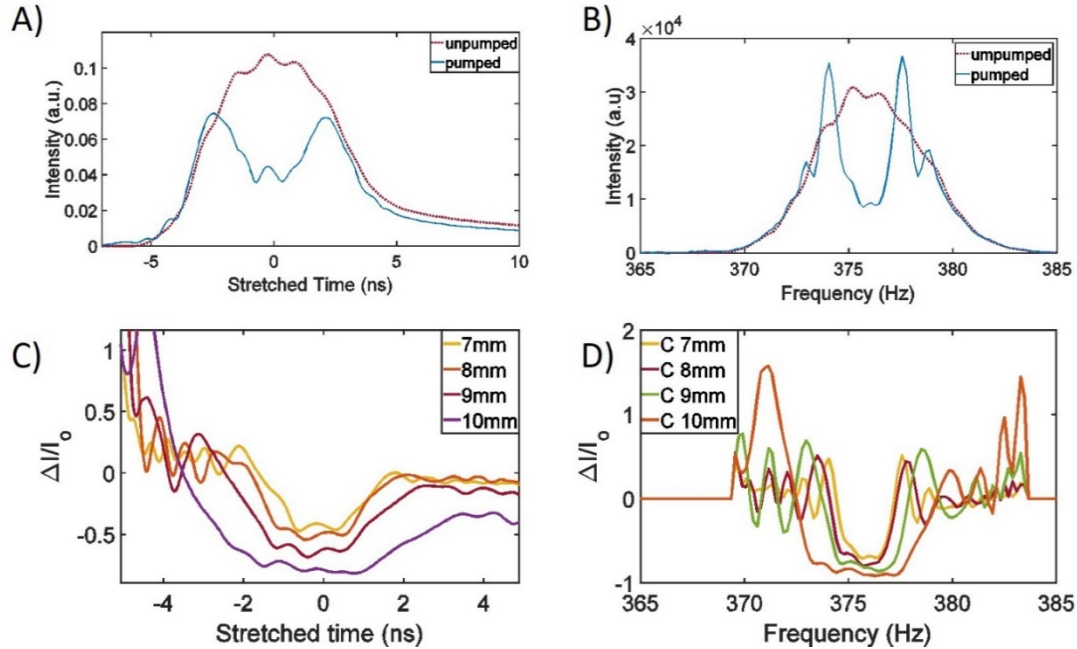

Figure 5.1: The pump on, pump off traces for both the fiber A) and the spectrometer B). In A), the x-axis denotes the ns time scale of the post-fiber stretched pulse. In B) we've converted the spectrometer data from wavelength to frequency, which is centered at 375 THz which is the frequency of the center 800nm wavelength. Both traces show a transient drop in intensity when the pump is on. C) and D) The $\Delta I/I_0$ signal response for the fiber and spectrometer at different compressor settings of the laser. As the time window is reduced, the signal becomes stretched further and further out in time or frequency.

The third measurement of the signal was a traditional stage-scan, pump-probe measurement with a Fourier transform limited probe pulse. The signal from this classic pump-probe measurement is shown in Figure 5.2A. We did a direct comparison to the signal we get from our single-shot setups shown in Figure 5.2B. The time scale on the single-shot measurements is changed due to the stretching of the probe pulse. To make a direct comparison we have to put the signal back into real time. By moving the probe pulse stage,

the pump pulse signal will show up at earlier or later on the probe pulse. From this we can determine the stage distance (and therefore real time delay) that equates to frequency or stretched time. After converting from the stretched time and frequency in Figures 5.1C and D to the ultrafast (real) time scale, we plot the single-shot signals in Figures 5.2B and C. Figure 5.2B shows the fiber and spectrometer single-shot signals for a compressor setting of 9.2 mm. Figure 5.2C shows the spectrometer single-shot signal (converted to real time) for 4 compressor settings in the spectrometer. The single-shot signals clearly do not look the same as the stage-scan measurement. Below we comment on why this is the case, as well as differences between fiber and spectrometer single-shot signals.

There are differences in the signal between all three of the measurements taken. Most notably are the oscillations surrounding the dips in the spectrometer and fiber/oscilloscope measurements in comparison to the stage-scan measurements. The oscillations can be understood as a result of time-bandwidth limitations in the stretched probe-pulse. In essence, there is not enough bandwidth in a 100-fs-slice of our stretched pulse to allow the measurement of 100 fs dynamics. The longer the fixed-bandwidth probe pulse is pre-stretched in time, the less bandwidth there is per 100-fs-slice. Our 100-fs pulse is about 10nm in bandwidth from 795-805 nm. That means that when we stretch the 10 nm of bandwidth out to the picosecond time scale, every 100-fs-section of the stretched pulse no longer has a full 10 nm of bandwidth.
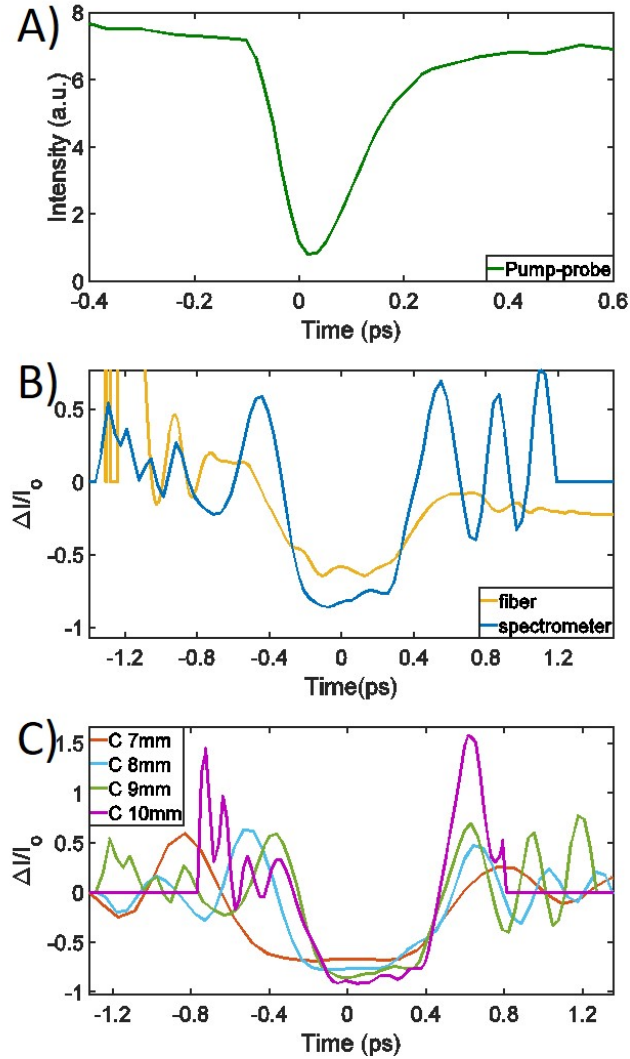
Figure 5.2: A) Illustrates a classic 800 nm pump-800 nm probe stage-scan measurement of excited carrier dynamics in GaP. B) The signal from both the spectrometer and the fiber measurements, with the x-axis converted to be real time. C) We show the spectrometer single-shot signal for different compressor settings.

This results in reducing the sensitivity to certain frequencies. This so-called

dispersion penalty can be described by a frequency domain transfer function [36]

$$H(f_m) = \cos(2\pi^2 \beta_2 L_1 f_m^2)$$
<div align="right">Eq 5.1</div>

β_2 is the dispersion coefficient of the fiber, L_1 is the length of the fiber, and f_m is the frequency to be detected. The transfer function is plotted as the red line in Figure 5.3. The periodic dips in this plot mean the certain frequencies will not be detectable in a spectral encoding measurement. Also in Figure 5.3 is the Fourier transforms of the signal that we get from the fiber (blue line) and spectrometer (green line). We see dips in approximately the same location that dips are in the transfer function. The lack of frequency information at these particular frequencies is what leads to the added oscillations in the time domain signal. If our sample response only had slow signal components with frequencies less than the first minimum in the transfer function, the single-shot signal would match well the stage-scan signal. But because our GaP signal has very short time, high-frequency components, the dispersion penalty modifies the observed single-shot signal.

We can estimate where the first minimum will appear in the frequency with the following equation [36].

$$f_{m0} \approx \frac{1}{\sqrt{4\pi\beta_2 L_1}}$$
<div align="right">Eq. 5.2</div>

This is an indication of the tradeoff between time resolution and the time window of your trace in the time domain. Knowing about this trade off and transfer function, we can back track out our true signal from the spectrometer and oscilloscope. The observed signal is the transfer function multiplied by the Fourier transform of the true signal.

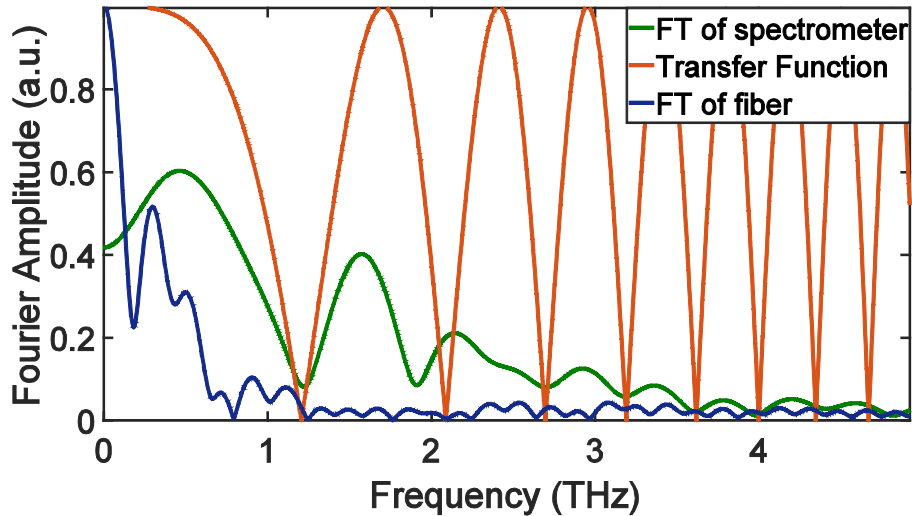$$S_{observed} = H(f_m) * S_{true} \qquad \text{Eq. 5.3}$$

Figure 5.3: Fourier transforms of the fiber and spectrometer data, green and blue lines respectively. The transfer function is also graphed (red line) showing the frequencies that are not captured due to the dispersion penalty.

Using this equation, we can recover the true signal we have if we divide our observed signal by the transfer function. This presents problems in that the transfer function has frequencies where it reaches 0, and dividing by zero is never a good idea. Alternatively, we are currently trying to model the true signal (to match Figure 5.2A), and then multiplying the Fourier transform of the model signal by the transfer function, and inverse transforming to match the detected signal. In Figure 5.4 we show the model true signal and the resulting single-shot signal using the transfer function from Figure 5.3. The modeled signal could then be adjusted to best match the recorded single shot signal.
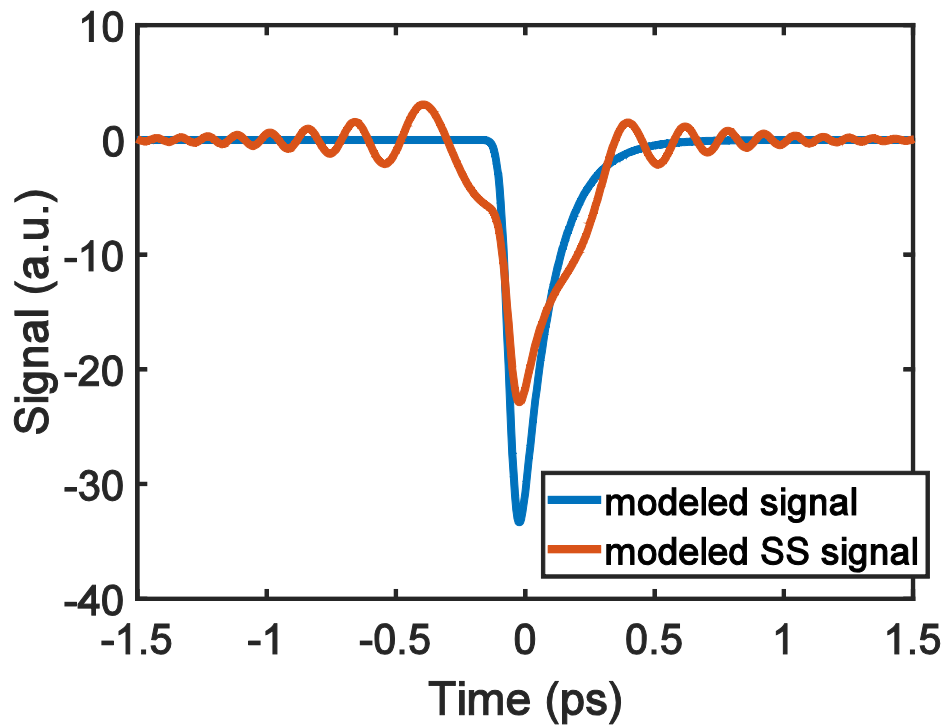
Figure 5.4 A plot of the modeled real signal, similar to Figure 5.2A, with the modeled single-shot (SS) signal. The SS model is made by multiplying the Fourier transform of the real signal by the transfer function, and then inverse Fourier transform to produce the SS signal.

With this project, we are hoping to improve our model signal so that the single-shot signal is more closely resembled; thus, we can accurately determine the true sample response. The other change that is needed is in the transfer function. The transfer function we used was derived for a similar experimental setup and conditions as ours, but there were some key differences that the model should be adjusted to account for. We need to adjust the transfer function to match our experiment more closely so that the minima in the frequency domain matches our dips in signal more closely. With these adjustments, it will allow us to more accurately recover the true signal we are attempting to measure in a single probe shot.

REFERENCES

1.	Muybridge, E., *Horse in Motion*, in *Library on Congress*. 1878.

2.	Bailey, G.W. and S.W. Karickhoff, *UV-VIS Spectroscopy in the Characterization of Clay Mineral Surfaces.* Analytical Letters, 1973. **6**(1): p. 43-49.

3.	Baker, M.J., et al., *Using Fourier transform IR spectroscopy to analyze biological materials.* Nat. Protocols, 2014. **9**(8): p. 1771-1791.

4.	Park, H., T.F. Gallagher, and P. Pillet, *Microwave pump-probe spectroscopy of the dipole-dipole interaction in a cold Rydberg gas.* Physical Review A, 2016. **93**(5): p. 052501.

5.	Lehmann, C.S., et al., *Ultrafast x-ray-induced nuclear dynamics in diatomic molecules using femtosecond x-ray-pump\char21{}x-ray-probe spectroscopy.* Physical Review A, 2016. **94**(1): p. 013426.

6.	Wu, Q. and X.C. Zhang, *Free-space electro-optic sampling of terahertz beams.* Applied Physics Letters, 1995. **67**(24): p. 3523-3525.

7.	Falicov, L.M. and P.J. Lin, *Band Structure and Fermi Surface of Antimony: Pseudopotential Approach.* Physical Review, 1966. **141**(2): p. 562-567.

8.	Yoshikawa, A., H. Matsunami, and Y. Nanishi, *Development and Applications of Wide Bandgap Semiconductors*, in *Wide Bandgap Semiconductors*. 2007, Springer. p. 1-24.

9.	Davis, U., *Metals and Semiconductors*. 2016, LibreTexts.

10.	Neudeck, P.G., R.S. Okojie, and C. Liang-Yu, *High-temperature electronics - a role for wide bandgap semiconductors?* Proceedings of the IEEE, 2002. **90**(6): p. 1065-1076.

11.	Lange, C., et al., *Extremely Nonperturbative Nonlinearities in GaAs Driven by Atomically Strong Terahertz Fields in Gold Metamaterials.* Physical Review Letters, 2014. **113**(22): p. 227401.

12.	Hirori, H., et al., *Extraordinary carrier multiplication gated by a picosecond electric field pulse.* 2011. **2**: p. 594.

13.	Kane, E.O., *Zener tunneling in semiconductors.* Journal of Physics and Chemistry of Solids, 1960. **12**(2): p. 181-188.

14.	Anderson, C.L. and C.R. Crowell, *Threshold Energies for Electron-Hole Pair Production by Impact Ionization in Semiconductors.* Physical Review B, 1972. **5**(6): p. 2267-2272.

15.	Fan, K., et al., *Nonlinear Terahertz Metamaterials via Field-Enhanced Carrier Dynamics in GaAs.* Physical Review Letters, 2013. **110**(21): p. 217404.

16.	Song, H.J. and T. Nagatsuma, *Present and Future of Terahertz Communications.* IEEE Transactions on Terahertz Science and Technology, 2011. **1**(1): p. 256-263.

17. Albrecht, J.D., et al. *THz Electronics projects at DARPA: Transistors, TMICs, and amplifiers*. in *2010 IEEE MTT-S International Microwave Symposium*. 2010.

18. Gadalla, M.N., M. Abdel-Rahman, and A. Shamim, *Design, Optimization and Fabrication of a 28.3 THz Nano-Rectenna for Infrared Detection and Rectification.* Scientific Reports, 2014. **4**: p. 4270.

19. Baliga, B.J., *Power semiconductor device figure of merit for high-frequency applications.* IEEE Electron Device Letters, 1989. **10**(10): p. 455-457.

20. Sekino, H. and R.J. Bartlett, *Frequency dependent nonlinear optical properties of molecules.* The Journal of Chemical Physics, 1986. **85**(2): p. 976-989.

21. Bloembergen, N., *Laser-induced electric breakdown in solids.* IEEE Journal of Quantum Electronics, 1974. **10**(3): p. 375-386.

22. Ueno, K., et al., *Electric-field-induced superconductivity in an insulator.* Nat Mater, 2008. **7**(11): p. 855-858.

23. Chow, T.P. and R. Tyagi. *Wide bandgap compound semiconductors for superior high-voltage power devices*. in *[1993] Proceedings of the 5th International Symposium on Power Semiconductor Devices and ICs*. 1993.

24. Werley, C.A., et al., *Time-resolved imaging of near-fields in THz antennas and direct quantitative measurement of field enhancements.* Optics Express, 2012. **20**(8): p. 8551-8567.

25. Sparks, M., et al., *Theory of electron-avalanche breakdown in solids.* Physical Review B, 1981. **24**(6): p. 3519-3536.

26. Lee, C.H., *Picosecond optoelectronic switching in GaAs* Applied Physics Letters, 1977. **30**(2): p. 84-86.

27. Brunner, F.D.J., et al., *A hydrogen-bonded organic nonlinear optical crystal for high-efficiency terahertz generation and detection.* Optics Express, 2008. **16**(21): p. 16496-16508.

28. Leitenstorfer, A., et al., *Detectors and sources for ultrabroadband electro-optic sampling: Experiment and theory.* Applied Physics Letters, 1999. **74**(11): p. 1516-1518.

29. Bube, R.H., *Photoelectronic Analysis of High Resistivity Crystals: (a) GaAs, (b) Sb2S3.* Journal of Applied Physics, 1960. **31**(2): p. 315-322.

30. Cohen, M.L. and T.K. Bergstresser, *Band Structures and Pseudopotential Form Factors for Fourteen Semiconductors of the Diamond and Zinc-blende Structures.* Physical Review, 1966. **141**(2): p. 789-796.

31. Buckley, B.W., A.M. Madni, and B. Jalali, *Coherent time-stretch transformation for real-time capture of wideband signals.* Optics Express, 2013. **21**(18): p. 21618-21627.

51

32.   Szwaj, C., et al., *High sensitivity photonic time-stretch electro-optic sampling of terahertz pulses.* Review of Scientific Instruments, 2016. **87**(10): p. 103111.

33.   Wesch, S., et al., *A multi-channel THz and infrared spectrometer for femtosecond electron bunch diagnostics by single-shot spectroscopy of coherent radiation.* Nuclear Instruments and Methods in Physics Research Section A: Accelerators, Spectrometers, Detectors and Associated Equipment, 2011. **665**: p. 40-47.

34.   Adam, J., et al., *Spectrally encoded angular light scattering.* Optics Express, 2013. **21**(23): p. 28960-28967.

35.   Kobayashi, M., et al., *High-Acquisition-Rate Single-Shot Pump-Probe Measurements Using Time-Stretching Method.* 2016. **6**: p. 37614.

36.   Gimlett, J. and C. Nim, *Dispersion penalty analysis for LED/single-mode fiber transmission systems.* Journal of Lightwave Technology, 1986. **4**(9): p. 1381-1392.

52